

# Time-dependent models of accretion disks formed from compact object mergers

B. D. Metzger<sup>\*</sup>, A. L. Piro, and E. Quataert

*Astronomy Department and Theoretical Astrophysics Center, University of California, Berkeley, 601 Campbell Hall, Berkeley CA, 94720*

Accepted . Received ; in original form

## ABSTRACT

We present time-dependent models of the remnant accretion disks created during compact object mergers, focusing on the energy available from accretion at late times and the composition of the disk and its outflows. We calculate the dynamics near the outer edge of the disk, which contains the majority of the disk’s mass and determines the accretion rate onto the central black hole. This treatment allows us to follow the evolution over much longer timescales (100 s or longer) than current hydrodynamic simulations. At late times the disk becomes advective and its properties asymptote to self-similar solutions with an accretion rate  $\dot{M}_d \propto t^{-4/3}$  (neglecting outflows). This late-time accretion can in principle provide sufficient energy to power the late-time activity observed by *Swift* from some short-duration gamma-ray bursts. However, because outflows during the advective phase unbind the majority of the remaining mass, it is difficult for the remnant disk alone to produce significant accretion power well beyond the onset of the advective phase. Unless the viscosity is quite low ( $\alpha \lesssim 10^{-3}$ ), this occurs before the start of observed flaring at  $\sim 30$  s; continued mass inflow at late times thus appears required to explain the late-time activity from short-duration gamma-ray bursts. We show that the composition of the disk freezes-out when the disk is relatively neutron rich (electron fraction  $Y_e \simeq 0.3$ ). Roughly  $10^{-2}M_\odot$  of this neutron-rich material is ejected by winds at late times. During earlier, neutrino-cooled phases of accretion, neutrino irradiation of the disk produces a wind with  $Y_e \simeq 0.5$ , which synthesizes at most  $\sim 10^{-3}M_\odot$  of  $^{56}\text{Ni}$ . We highlight what conditions are favorable for  $^{56}\text{Ni}$  production and predict, in the best cases, optical and infrared transients peaking  $\sim 0.5 - 2$  days after the burst, with fluxes a factor of  $\sim 10$  below the current observational limits.

**Key words:** accretion disks — black hole physics — gamma rays: bursts — neutrinos

## 1 INTRODUCTION

The most popular model for the creation of short duration gamma-ray bursts (GRBs) is either binary neutron star (NS/NS) or black hole-neutron star (BH/NS) coalescence (Paczynski 1986, 1991; Eichler et al. 1989; Narayan et al. 1991). Support for the merger hypothesis comes from their durations of  $\lesssim 2$  s, observations of well-localized short GRBs in galaxies without strong star formation (Berger et al. 2005; Gehrels et al. 2005; Hjorth et al. 2005), and the lack of a detectable coincident supernovae (Hjorth et al. 2005; Bloom et al. 2006; Soderberg et al. 2006; Ferrero et al. 2007), as is found in the

case of long ( $\gtrsim 2$  s) GRBs (Galama et al. 1998; Hjorth et al. 2003; Stanek et al. 2003).

Previous theoretical studies of the merger process have focused on one of two stages. The first is the *dynamical* portion in which the less massive companion is tidally disrupted by the more massive BH (Lee & Kluźniak 1995, 1998, 1999; Kluźniak & Lee 1998; Janka et al. 1999; Rosswog et al. 2004) or NS (Ruffert et al. 1996; Ruffert & Janka 1999; Oechslin & Janka 2006). The details of whether a dynamical instability (Rasio & Shapiro 1994; Lai et al. 1994) or Roche lobe overflow occurs depends on the mass ratio and the nuclear equation of state (Bildsten & Cutler 1992; Uryū & Eriguchi 1999).

Nevertheless, generally  $\sim 0.01 - 0.1M_\odot$  of material remains in a remnant disk following the dynamical stage. The accretion of this material onto the central object gives rise to the second, *disk* portion of the merger. The ener-

<sup>\*</sup> E-mail: bmetzger@astro.berkeley.edu

getics and timescale of the accretion phase are reasonably consistent with observations of short GRBs, as was shown by models of steady-state, azimuthally symmetric, vertically averaged disks (Popham et al. 1999; Narayan et al. 2001; Kohri & Mineshige 2002; DiMatteo et al. 2002; Chen & Beloborodov 2007). More recently, these disks have been modeled with time-dependent calculations in 1D (Janiuk et al. 2004), 2D (Lee et al. 2004, 2005b), and 3D (Setiawan et al. 2004, 2006). The typical time interval that present multi-dimensional calculations can simulate is on the order of the burst duration or less ( $\sim 1 - 2$  s for 2D and  $\sim 50$  ms for 3D).

Recent observations of short GRBs by *Swift*, however, indicate continued activity from the central engine on much longer timescales. X-ray flares with durations of  $\sim 100$  s after a delay of  $\sim 30$  s have been seen from several bursts (Barthelmy et al. 2005; Villaseñor et al. 2005; Campana et al. 2006; La Parola et al. 2006). Stacked lightcurves of many bursts indicate continued activity on a similar timescale (Lazzati et al. 2001; Montanari et al. 2005). In one extreme case, GRB 050724 displayed an X-ray flare 12 hours post-burst. This flaring activity has been attributed to a number of different sources, including fragmentation of a rapidly rotating core (King et al. 2005), magnetic regulation of the accretion flow (Proga & Zhang 2006), fragmentation of the accretion disk (Perna et al. 2005; although this explanation may have difficulty reproducing the observed timescales, Piro & Pfahl 2007), differential rotation in a post-merger millisecond pulsar (Dai et al. 2006), and an infalling tidal tail of material stripped from the disrupted NS (Lee & Ramirez-Ruiz 2007; Rosswog 2007).

In order to determine whether the late-time activity from short GRBs is consistent with a compact merger origin, the disk evolution should be followed for timescales much longer than the initial viscous time. With this aim, we perform time-dependent calculations modeling the disk as an annulus that contains the majority of the mass. This simplification allows us to study the disk evolution for arbitrarily long timescales, and to readily determine important properties such as the disk’s composition and when it becomes advective. We are also able to survey much of the parameter space of initial disk mass and angular momentum. In §2 we discuss the initial conditions for disks formed from compact object mergers. This is followed by §3, in which we summarize the main assumptions of our ring model. In §4 we present the results of our calculations and summarize the main properties of the models. We then calculate outflows from our disk solutions in §5. We investigate the composition of the outflows and argue that they generally consist of neutron-rich isotopes, but can produce  $^{56}\text{Ni}$  in some circumstances. The presence or lack of an optical transient from short GRBs therefore provides an important constraint on progenitor models. We conclude in §6 with a discussion of our results. In Appendix A we summarize the Green’s function solution to the viscous spreading of a ring, which is important for connecting our ring model to the true extended disk geometry. In Appendix B we present analytic self-similar solutions that reproduce many of the features of our numerical solutions.

## 2 INITIAL CONDITIONS

The dynamical phase of NS/NS or BH/NS mergers has been studied extensively using a number of different numerical techniques and methods for including general relativity (GR). Here we summarize some of the most relevant features for our study (for a more detailed review, see Lee & Ramirez-Ruiz 2007).

When the lighter companion NS is first tidally disrupted, a debris disk is formed within only a few dynamical timescales. The initial disk mass,  $M_{d,0}$ , is generally larger for more asymmetric mass ratios (i.e., small  $q$ , where  $q$  is the ratio of the lighter to the heavier binary component). For example, Shibata & Taniguchi (2006) find that for a NS/NS merger with  $q = 0.7$  that  $M_{d,0} = 0.03 M_{\odot}$ , but for  $q = 0.9$  the disk is much less massive with  $M_{d,0} = 10^{-3} M_{\odot}$ . Another trend is that including strong gravity gives less massive remnant disks. The BH spin is also important, with larger spin favoring disk formation (Rasio et al. 2005) and the production of a tidal tail. These have masses of  $\simeq 0.01 - 0.05 M_{\odot}$  and may provide prolonged mass inflow (Lee & Ramirez-Ruiz 2007), but for simplicity this will be ignored here. Taken together, these simulations generally find  $M_{d,0} \simeq 0.01 - 0.3 M_{\odot}$ , with the disk containing a substantial fraction of the angular momentum of the disrupted companion.

In the standard picture of NS-NS mergers, the resulting hypermassive NS collapses to a BH shortly following the merger. However, simulations show that when (and if) collapse actually occurs depends on the mass of the central NS and its ability to transport angular momentum to the surrounding disk (Shibata et al. 2005; Shibata & Taniguchi 2006; Shibata et al. 2006). In fact, if the NS remains supported by differential rotation for several seconds (Baumgarte et al. 2000; Morrison et al. 2004; Duez et al. 2004, 2006) or loses sufficient mass via a centrifugally-driven outflow (e.g., Thompson et al. 2004; Dessart et al. 2008a), the NS itself may power the GRB (e.g., Price & Rosswog 2006). In this paper we assume that the central object promptly collapses to a BH; our model, however, would be reasonably applicable for the case of a central NS as well, the primary difference being that the significant neutrino flux from the newly-formed NS and from the boundary layer between the disk and the NS could modify the composition and thermal properties of the disk.

We present some characteristic numbers to motivate our choice of initial conditions. Consider a binary with masses  $M$  and  $m$  ( $M > m$ ), where the latter is the NS (with radius  $R$ ) that is tidally disrupted. The disruption radius,  $a_t$ , is estimated to be (Kopal 1959, adding Fishbone’s 1973 10% strong gravity correction)

$$a_t \simeq 2.4R \left( \frac{M+m}{m} \right)^{1/3}. \quad (1)$$

The characteristic orbital period at this radius is

$$P_t \simeq 23.4 \left( \frac{R^3}{Gm} \right)^{1/2} \simeq 2 \times 10^{-3} m_{1.4}^{-1/2} R_6^{3/2} \text{ s}, \quad (2)$$

where  $m_{1.4} = m/1.4 M_{\odot}$  and  $R_6 = R/10^6$  cm, with an orbital angular momentum of

$$J_t = (G(M+m)a_t)^{1/2} m$$

$$\simeq 6 \times 10^{49} (1/q + 1)^{2/3} m_{1.4}^{3/2} R_6^{1/2} \text{ ergs s}, \quad (3)$$

where  $q = m/M$ . The disrupted NS also contains spin angular momentum. This is negligible since the NS is not strongly affected by tidal coupling (Bildsten & Cutler 1992). Even a rapidly rotating NS ( $\simeq 5$  ms) has an associated angular momentum of merely  $\sim 10^{48}$  ergs s.

Once disrupted, a considerable fraction of the NS is either lost from the system or immediately swallowed by the BH. The remaining material forms a thick torus surrounding the central BH. Its associated viscous timescale can be estimated by assuming that the majority of the torus' mass lies at a single radius,  $r_{d,0}$ . Taking the angular momentum of the disk to be  $J_d \simeq (GM r_{d,0})^{1/2} M_{d,0}$ , we estimate

$$r_{d,0} \simeq 3 \times 10^7 M_3^{-1} M_{0.1}^{-2} \left( \frac{J_{49}}{2} \right)^2 \text{ cm}, \quad (4)$$

where  $M_3 = M/3 M_\odot$ ,  $M_{0.1} = M_{d,0}/0.1 M_\odot$ , and  $J_{49} = J_d/10^{49}$  ergs s. For a disk with half-thickness  $H$ , the viscous timescale is

$$\begin{aligned} t_{\text{visc},0} &= \alpha^{-1} \left( \frac{r_d}{H} \right)^2 \left( \frac{r_d^3}{GM} \right)^{1/2} \\ &\simeq 6 \times 10^{-2} \alpha_{0.1}^{-1} M_3^{-1/2} r_7^{3/2} \left( \frac{H}{0.5 r_d} \right)^{-2} \text{ s}, \end{aligned} \quad (5)$$

where  $\alpha = 0.1 \alpha_{0.1}$  is the standard dimensionless viscosity (Shakura & Sunyaev 1973),  $r_7 = r_{d,0}/10^7$  cm, and we have scaled to an initial ratio of  $H/r_d = 0.5$ , consistent with our numerical solutions. The initial viscous time  $t_{\text{visc},0}$  is roughly the time at which the central BH begins accreting in earnest. The strong dependence of  $t_{\text{visc},0}$  on disk mass and radius demonstrates that the initial evolution of the disk is sensitive to the outcome of the dynamical phase of the merger. But as we will show, the late time evolution is much less sensitive to initial conditions and is well described by self-similar solutions.

### 3 PHYSICS OF THE EXPANDING RING MODEL

Given these initial conditions, one would like to know how the disk then evolves. Modeling the entire disk requires resolving timescales over  $\sim 4 - 6$  orders of magnitude. This makes it expensive to carry out simulations for long periods of time. We consider instead a simplified model that captures most of the features of interest. At any given time,  $t$ , the disk can be broken into three regions depending on the local viscous time,  $t_{\text{visc}}$ , which increases with radius, roughly as  $t_{\text{visc}} \sim r^{3/2}$ . At small radii,  $t_{\text{visc}} < t$ , and the disk comes into steady-state. This is the region most often modeled in previous studies (Popham et al. 1999; Narayan et al. 2001; Kohri & Mineshige 2002; DiMatteo et al. 2002; Chen & Beloborodov 2007). The radii where  $t_{\text{visc}} \sim t$  contain the majority of the disk's mass and angular momentum. Therefore, this region determines the viscous evolution of the rest of the disk, including the mass accretion rate that is fed to the interior steady-state region. Motivated by this fact, we focus on this radius and model the disk as a ring. Exterior to this point is a third region where  $t_{\text{visc}} > t$ , but this contains a small amount of mass and is negligible for the viscous evolution.

### 3.1 Dynamical Equations

Our ring model treats the disk as a single annulus that is evolved forward in time. In this picture, the properties of the ring, such as its surface density  $\Sigma$  and temperature  $T$ , are representative of the location where  $\Sigma r^2$  peaks. The main drawback of this method is that the material in the disk is in fact distributed spatially in radius. Thus, although the mass of the disk in the vicinity of  $r_d$  is  $\simeq \pi \Sigma r_d^2$ , the total mass of the disk (integrated over all radii) is  $M_d = A \pi \Sigma r_d^2$ , where  $A$  is a factor of order unity that accounts for the distinction between the total mass of the disk and the mass of the material near  $r_d$ . Similarly, we write the total angular momentum of the disk as  $J_d = B (GM r_d)^{1/2} \pi r_d^2 \Sigma$ . At early times the constants  $A$  and  $B$  depend on the initial conditions of how matter is spatially distributed; however, at times much greater than the initial viscous time (given by eq. [5]), material initially concentrated at a given radius becomes spread out in a manner determined by the viscosity. As described in detail in Appendix A, we choose the constants  $A$  and  $B$  by setting the solution of our simplified ring model at late times equal to the Green's function solution for a spreading ring with a viscosity  $\nu \propto r^{1/2}$  (as is appropriate for the radiatively inefficient disk at late-times). This fixes  $A = 3.62$  and  $B = 3.24$ .<sup>1</sup> Conveniently  $A/B \simeq 1$ , so that it is a good approximation to take  $J_d \simeq (GM r_d)^{1/2} M_d$ .

The time evolution of the disk is determined by the conservation equations. Conservation of mass is

$$\frac{d}{dt} (A \pi \Sigma r_d^2) = -\dot{M}_d, \quad (6)$$

where  $\dot{M}_d$  is in general the total mass loss rate, which could include both accretion and a wind (for now we ignore the effects of a wind). Conservation of angular momentum is

$$\frac{d}{dt} [B (GM r_d)^{1/2} \pi \Sigma r_d^2] = -\dot{J}, \quad (7)$$

where  $\dot{J}$  is the angular momentum loss rate. Equations (6) and (7) provide two coupled equations that can be solved for the dependent variables  $r_d$  and  $\Sigma$ .

The accretion rate must depend on the characteristic mass and viscous timescale of the ring, so we use

$$\dot{M}_d = f M_d / t_{\text{visc}}, \quad (8)$$

where  $t_{\text{visc}} = r_d^2 / \nu$  and  $\nu$  is the viscosity. The factor  $f$  is set like  $A$  and  $B$  to match the exact solution of a spreading ring with  $\nu \propto r^{1/2}$  (Appendix A), which gives  $f = 1.6$ .<sup>2</sup> Requiring a no-torque boundary condition at a radius  $r_*$ , we take

$$f = 1.6 / [1 - (r_*/r_d)^{1/2}]. \quad (9)$$

In contrast, a steady-state disk obeys  $\dot{M}_d = 3\pi\nu\Sigma$  (ignoring the no-torque condition), which instead gives  $f = 3/A \simeq 0.83$ .

For the viscosity, we use an  $\alpha$ -prescription,

$$\nu = \alpha c_s H, \quad (10)$$

<sup>1</sup> In fact, when the total angular momentum is conserved, the viscous evolution is independent of  $A/B$  as long as  $A/B$  is nearly constant with time.

<sup>2</sup> Although we set  $t_{\text{visc}} = r^2/\nu$ , any prefactors that could go into this prescription would just be absorbed into a re-definition of  $f$ .

where  $c_s = (P/\rho)^{1/2}$  is the isothermal sound speed. The equation of state includes contributions from radiation pressure, gas pressure, relativistic degeneracy pressure, and neutrino pressure as in DiMatteo et al. (2002).

### 3.2 Energetics

For the energy equation, we take

$$q_{\text{visc}} = q_{\nu}^{-} + q_{\text{adv}}, \quad (11)$$

where  $q_{\text{visc}}$  is the viscous heating,  $q_{\nu}^{-}$  is the neutrino cooling (using the prescriptions given by DiMatteo et al. 2002, which includes neutrino optical-depth effects),  $q_{\text{adv}}$  is the advective heat flux, and all  $q$  values correspond to half the disk thickness.

For a disk rotating at the Keplerian frequency  $\Omega = (GM/r_d^3)^{1/2}$ ,

$$q_{\text{visc}} = \frac{9}{8}\nu\Omega^2\Sigma = \frac{9}{8fA}\frac{GM\dot{M}_d}{\pi r_d^3}\left[1 - \left(\frac{r_*}{r_d}\right)^{1/2}\right], \quad (12)$$

where the prefactor  $9/(8fA) \simeq 0.2$  is different from the steady-state value of  $3/8$ . The advective term,  $q_{\text{adv}}$ , is set as in DiMatteo et al. (2002), with the only difference being that the radial velocity is the expansion rate of the ring's radius

$$V_r = \frac{dr_d}{dt} = \frac{2\dot{M}}{A\pi r_d\Sigma}, \quad (13)$$

where we have taken  $\dot{J} = 0$ .

Fusion to  $\alpha$ -particles produces heating in addition to  $q_{\text{visc}}$ , with

$$q_{\text{nucl}} = 6.8 \times 10^{28} \rho_{10} \frac{dX_{\alpha}}{dt} H, \quad (14)$$

where all quantities are expressed in cgs units,  $\rho_{10} = \rho/10^{10} \text{ g cm}^{-3}$  and  $X_{\alpha}$  is the mass fraction of  $\alpha$ -particles. Note that in our case  $q_{\text{nucl}} > 0$  since  $\alpha$ -particles are synthesized as the disk expands (in contrast to studies that follow cooling from photodisintegration as material moves inward). In our calculations we do not include  $q_{\text{nucl}}$  in solving equation (11) because we were not able to find reasonable solutions when doing so (for reasons explained in §4.1).

### 3.3 Composition

An advantage of the ring model is that other properties of the disk, such as its composition, can be cast into differential equations and integrated along with equations (6) and (7). Since the neutron content of the disk is particularly important for determining the properties of the disk's outflows, we evolve the electron fraction  $Y_e$  using

$$\frac{dY_e}{dt} = -Y_e r_{e-p} + (1 - Y_e) r_{e+n}, \quad (15)$$

where  $Y_e = X_p/(X_n + X_p)$ ,  $X_p$  and  $X_n$  are the proton and neutron mass fraction, respectively, and  $r_{e-p}$  and  $r_{e+n}$  are the electron and positron capture rates, respectively (Beloborodov 2003a). We have neglected the effect of neutrino absorptions on the evolution of  $Y_e$  in equation (15). Although absorptions are important at early times when the disk is optically thick, we are primarily concerned with the

late-time value of  $Y_e$ , which does not depend sensitively on the neutrino irradiation (see §4.2).

As the disk evolves, the protons and neutrons eventually burn to form  $\alpha$ -particles. At these times the disk is sufficiently cold that the positron and electron capture rates are negligible (i.e.,  $1/r_{e-p} \gg t_{\text{visc}}$ ) and  $Y_e$  has frozen-out. This fixes the difference between the free neutron and proton mass fractions

$$X_n - X_p = 1 - 2Y_e. \quad (16)$$

Since the rates for reactions that synthesize and destroy  $\alpha$ -particles are all fast in comparison to the viscous time, we determine the composition using nuclear statistical equilibrium (NSE) between protons, neutron, and  $\alpha$ -particles. This is expressed by the Saha relation (Shapiro & Teukolsky 1983)

$$X_p^2 X_n^2 = 1.57 \times 10^4 X_{\alpha} \rho_{10}^{-3} T_{10}^{9/2} \exp\left(-\frac{32.81}{T_{10}}\right). \quad (17)$$

NSE is a good assumption because the disk temperature is generally  $\gtrsim 0.5$  MeV (see Fig. 2), except at very late times or for very low disk masses (e.g., the  $M_{d,0} = 0.03M_{\odot}$  case, for which we do not calculate the nuclear composition anyways). By combining equations (16) and (17) with mass conservation,  $X_p + X_n + X_{\alpha} = 1$ , we solve for all of the mass fractions at a given  $\rho$ ,  $T$ , and  $Y_e$ .

## 4 TIME-EVOLVING SOLUTIONS

We next present the results of integrating equations (6), (7), and (15) forward in time. For simplicity, we typically assume that  $\dot{J} = 0$ . A convenient property of our formalism is the ease with which these complications can be included (for example, we consider the effects of winds at the end of §4.1). The disk properties are determined by the initial conditions  $M_{d,0}$ ,  $J_d$ , and  $Y_{e,0}$ , and by the viscosity  $\alpha$ . For the majority of our study we set the initial  $Y_{e,0} = 0.1$ , which is characteristic of the inner neutron star crust (Haensel & Zdunik 1990a,b; Pethick & Ravenhall 1995). An additional important parameter is  $r_*$ , which is set by the spin of the central BH. In most of our calculations we take  $r_* \simeq 2.3r_g \simeq 1.02 \times 10^6$  cm, corresponding to the innermost stable circular orbit of a  $3 M_{\odot}$  BH with spin  $a \simeq 0.9$ ; when calculating the properties of disk outflows in §5, however, we also consider the case of a nonrotating ( $a = 0$ ) BH. We consider the general evolution of the disk in §4.1, and then focus on the composition in §4.2.

### 4.1 Disk Evolution and Energetics

At any given time, a ring model is in one of three phases: (1) early-time, optically thick to neutrinos and advectively dominated, (2) mid-time, optically thin to neutrinos and geometrically thin, and (3) late-time, radiatively-inefficient accretion flow (RIAF).<sup>3</sup> This is analogous to the different regions of steady-state, hyper-accreting accretion disks (see,

<sup>3</sup> An optically thick, geometrically thin stage occurs between stages (1) and (2); however, this phase is brief and is not dynamically very different from phase (2), so we do not consider it separately in our discussion.

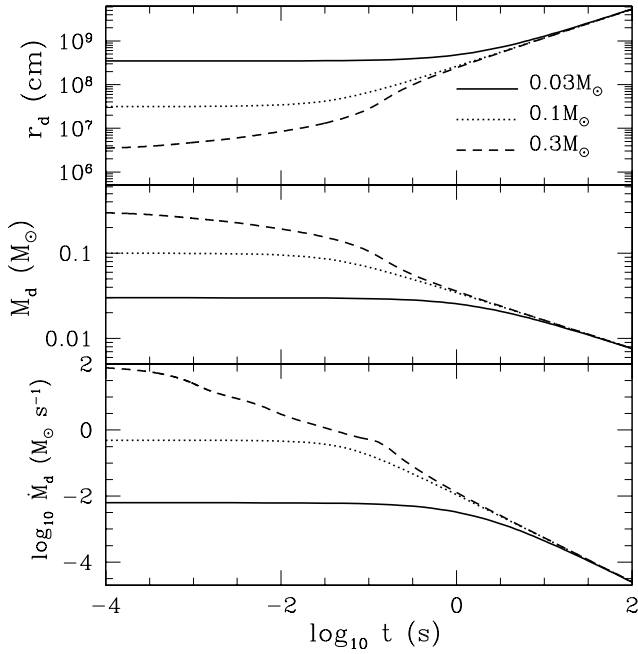


**Figure 1.** Example disk models showing the evolution of the disk radius,  $r_d$ , disk mass,  $M_d$ , and accretion rate,  $\dot{M}_d$ , as a function of time. We compare  $M_{d,0} = 0.03$  (solid lines),  $0.1$  (dotted lines) and  $0.3 M_\odot$  (dashed lines) solutions; all use  $J_{49} = 2$  and  $\alpha = 0.1$ . The inner radius is  $r_* \simeq 2.3r_g \simeq 1.02 \times 10^6$  cm (corresponding to a  $3 M_\odot$  BH with a spin of  $a \simeq 0.9$ ).

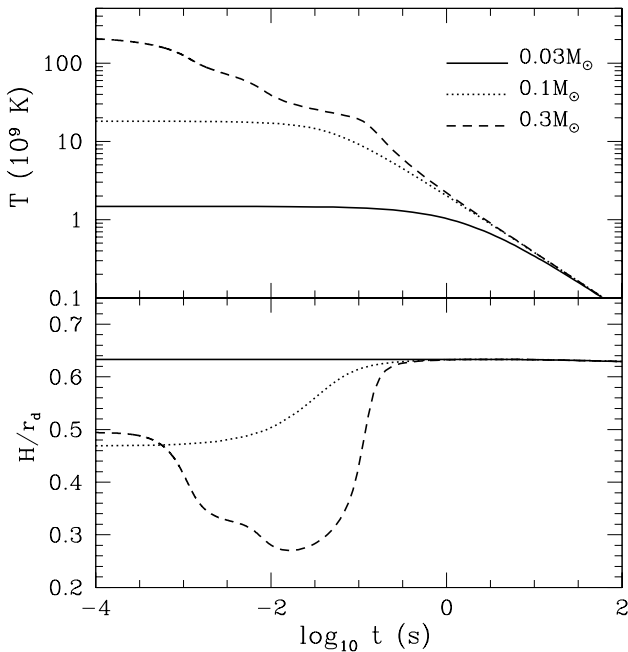


**Figure 2.** Comparison of the midplane temperatures and scaleheight for the three models from Fig. 1. In the lowest mass model, the ring is always advectively-dominated, thus  $H/r_d$  is constant.

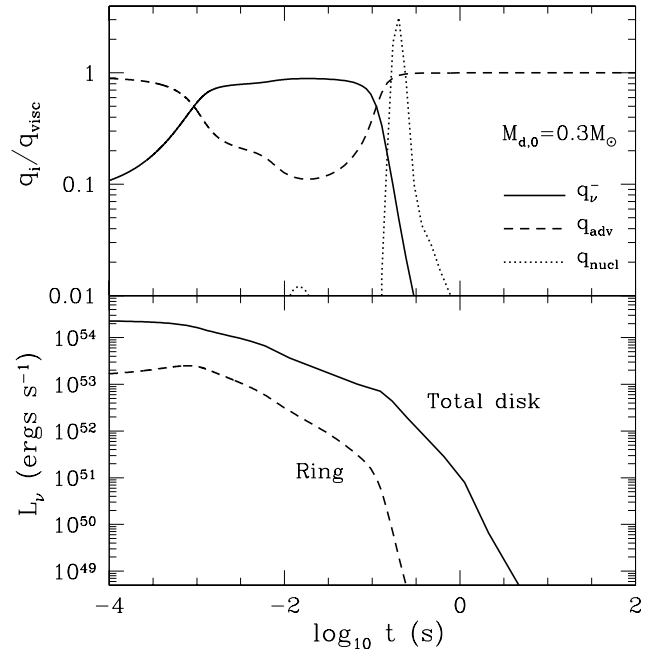


**Figure 3.** The cooling rates and neutrino luminosity for the  $M_{d,0} = 0.3 M_\odot$  model from Fig. 1. For the cooling rates we compare the neutrino (solid line) and advective (dashed line) rates, normalized to the viscous heating. The implied heating from the creation of  $\alpha$ -particles is plotted as a dotted line, but is not accounted for in the disk evolution. The neutrino luminosities are from the entire disk (solid line) and the ring (dashed line). The former luminosity is estimated by integrating over a steady-state disk model at each time given  $\dot{M}_d(t)$ .

e.g., Chen & Beloborodov 2007), but now the transitions occur with time instead of radius. The phases that a certain ring model samples during the course of its viscous expansion depends on  $t_{\text{visc},0}$ . A more compact disk (a shorter  $t_{\text{visc},0}$ ) will exhibit all three phases, while larger disks may only exhibit phases (2) and (3), or even just (3).

We present a number of figures that are helpful in understanding these three phases and how they are affected by changing  $M_{d,0}$ . Figure 1 shows the radius  $r_d$ , mass  $M_d$ , and accretion rate  $\dot{M}_d$  as a function of time, for  $M_{d,0} = 0.3, 0.1$ , and  $0.03 M_\odot$ . Figure 2 compares the midplane temperature and scaleheight for these same models. Figures 3 and 4 show key results describing the energetics of the  $M_{d,0} = 0.3$  and  $0.1 M_\odot$  solutions, respectively, while Figure 5 shows the different contributions to the total pressure in the disk as a function of time. Note that we fix the total angular momentum in these calculations ( $J_{49} = 2$ ) and thus a larger  $M_{d,0}$  corresponds to a smaller  $r_{d,0}$  and a shorter  $t_{\text{visc},0}$ .

The first transition the disks make is from an optically thick, advective disk to a thin, neutrino-cooled disk; i.e., from phase (1) to (2). This is only exhibited by the  $M_{d,0} = 0.3 M_\odot$  model and is seen most clearly at early times in Figure 2 when  $H/r_d \simeq 0.5$  and in Figure 3 when  $q_{\text{adv}} \gg q_\nu^-$ . Figure 5 shows that this phase is ion pressure (ideal gas) dominated. A simple estimate determines what initial disk mass is required for phase (1) to occur, i.e., for the initial disk to be optically thick and advective. The disk is advective for radii inside of which the neutrino diffusion

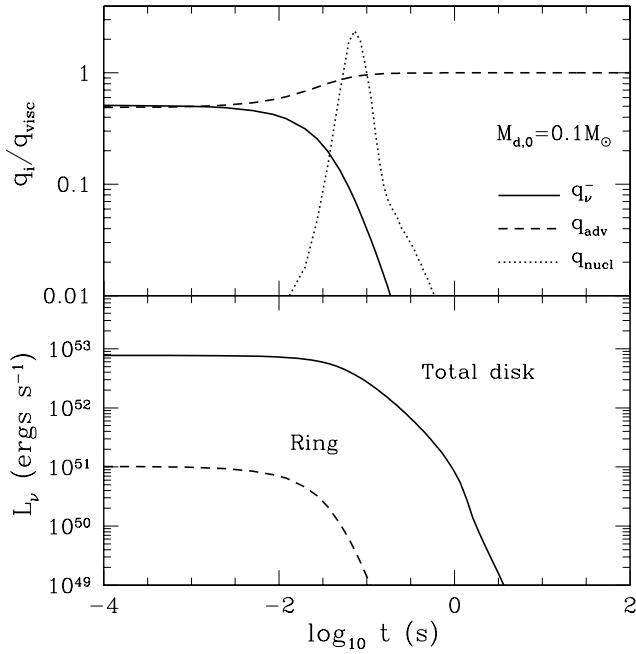


**Figure 4.** The same as Fig. 3, but for  $M_{d,0} = 0.1M_{\odot}$ .

time out of the disk exceeds the inflow time. Setting this radius equal to the initial radius of the disk (eq. [4]), we find that there is a critical disk mass below which the disk never experiences phase (1),

$$M_{d,crit} \sim 0.2\alpha_{0.1}^{-1/10} M_3^{-7/10} \left(\frac{J_{49}}{2}\right)^{9/10} \left(\frac{H}{0.5r_d}\right)^{-3/5} M_{\odot}, \quad (18)$$

where we have dropped scalings with  $f$  and  $A$  since they appear raised to the  $1/10$  power. This estimate is consistent with the fact that our  $M_{d,1} = 0.1M_{\odot}$  model is not advective at early times, as seen in Figures 2 and 4. In this case only phases (2) and (3) are seen, i.e., the disk is initially thin and neutrino cooled and later transitions to being advective.

Once the models reach the late-time, RIAF phase, or phase (3), they asymptote to self-similar solutions, independent of the initial disk mass. In this phase, the disk has  $q_{adv} > q_{\nu}^{-}$  and is radiation pressure dominated. We derive analytic self-similar solutions in Appendix B2 for this limit and show that  $r_d \propto t^{2/3}$ ,  $M_d \propto t^{-1/3}$  and  $\dot{M}_d \propto t^{-4/3}$ . The RIAF solution occurs external to an “ignition radius,” which we estimate as the location where the pair capture cooling rate balances  $\sim 1/2$  of the viscous heating for a thick disk,

$r_{ign} \simeq$

$$3 \times 10^7 \alpha_{0.1}^{-2} M_3^{-3/5} \left(\frac{H/r_d}{0.4}\right)^{-14/5} \left(\frac{\dot{M}_d}{0.1M_{\odot} s^{-1}}\right)^{6/5} \text{ cm}, \quad (19)$$

where we have scaled  $H/r_d$  to  $\approx 0.4$ , a value appropriate for the transition between the thin and thick disk regimes. We combine this with the analytic results for  $r_d(t)$  and  $\dot{M}_d(t)$  in the RIAF limit (eqs. [B7] and [B6])<sup>4</sup> to estimate the time when the disk transitions to being thick, which yields

<sup>4</sup> We use these solutions rather than the thin-disk ones because the numerical results follow these more closely (Fig. B1).

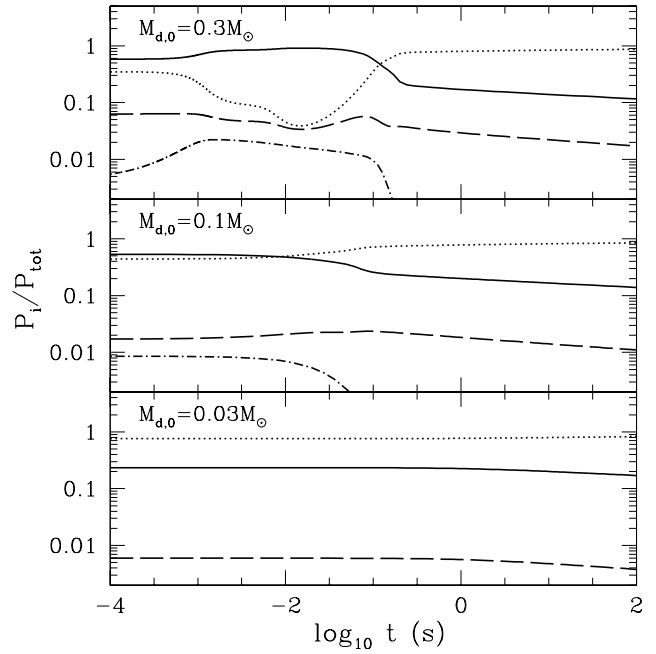


**Figure 5.** Pressure contributions for  $M_{d,0} = 0.3M_{\odot}$  (top panel),  $0.1M_{\odot}$  (middle panel) and  $0.03M_{\odot}$  (bottom panel). The pressures are all normalized to the total pressure and include the ion pressure (solid lines), radiation pressure (dotted lines), degenerate electron pressure (dashed line), and neutrino pressure (dot-dashed line).

$$t_{thick} \sim 0.1\alpha_{0.1}^{-23/17} M_3^{-13/17} \left(\frac{J_{49}}{2}\right)^{9/17} \text{ s}. \quad (20)$$

Equation (20) is only applicable if the disk is thin at early times. For sufficiently small initial disk masses, less than

$$M_{d,thick} \sim 0.1\alpha_{0.1}^{2/17} M_3^{-7/17} \left(\frac{J_{49}}{2}\right)^{14/17} M_{\odot}, \quad (21)$$

this is no longer true, and the disk is always a RIAF at its outer radius.

Figures 3 and 4 show that at approximately the same time as the disk transitions from being thin to thick, protons and neutrons are fused to He. Although the nuclear heating rate  $q_{nuc}$  is shown in Figures 3 and 4, this heating was not included in our time-dependent calculations so that we could obtain solutions at late times. The nuclear heating rate is sufficiently large, i.e.  $q_{nucl} \gtrsim q_{visc}$ , that the disk is not able to accommodate this added energy (it is already thick with  $H \simeq r$  due to viscous heating alone). This probably implies that the burning contributes to driving a powerful wind (as described by Lee & Ramirez-Ruiz 2007).

However, such a wind already begins at this time by virtue of the disk being advective (as discussed in §5.2). In Appendix B3, we present analytic self-similar solutions for advective disks with mass loss and show that this significant mass loss causes  $M_d$  and  $\dot{M}_d$  to decline much more rapidly with time than is shown in Figure 1. This is shown explicitly in Figure 6, where we present disk models calculated using the mass and angular momentum loss prescriptions described in Appendix B3; such losses are assumed to occur only when the disk is thick, between  $\sim \max(r_*, r_{ign})$  and  $\sim r_d$ . Figure 6 compares time-dependent solutions with

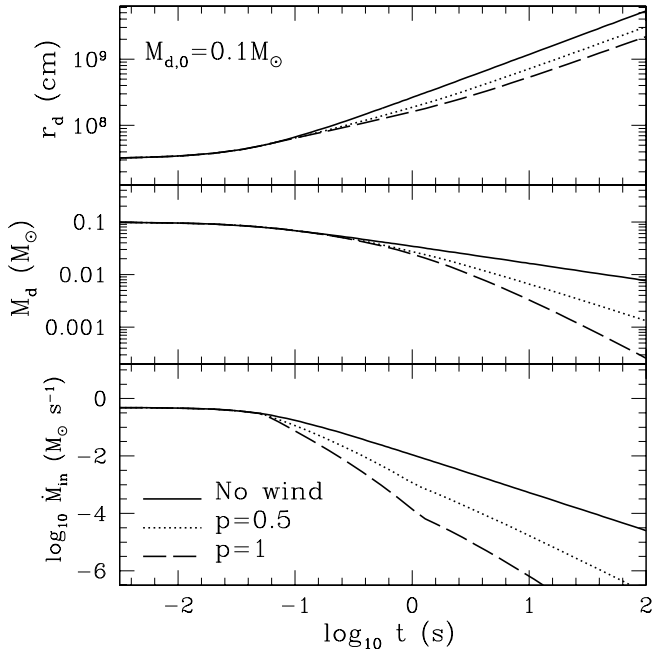


**Figure 6.** The radius  $r_d$ , disk mass  $M_d$ , and mass accretion rate reaching the central BH  $\dot{M}_{\text{in}}$  for different parameterizations of mass loss during the advective phase. We initialize a disk with  $M_{d,0} = 0.1 M_{\odot}$  (and all other parameters fixed as in Fig. 1) and compare solutions with no wind (solid line),  $p = 0.5$  (dotted line; see eq. [B8]), and  $p = 1$  (dashed line).

no wind (solid line), a wind with  $p = 0.5$  (dotted line; see eq. [B8]), and a wind with  $p = 1$  (dashed line).<sup>5</sup> The loss of angular momentum does not appreciably slow the radial expansion of the disk, but it does substantially accelerate the decline in the disk mass and accretion rate (see also eqs. [B12] and [B13]). If the models with winds are accurate, significant accretion is only likely to last for a few viscous times once the disk enters the late-time advective phase. Continued central engine activity at much later times could result from late-time infall of tidally stripped NS material (e.g., Lee & Ramirez-Ruiz 2007).

As an additional comparison, we present the effect of varying  $J_d$  in Figure 7. The main trend is that a higher  $J_d$  has a larger initial radius for a given  $M_d$ , and therefore a longer viscous time and smaller accretion rate. The late time behavior is more sensitive to  $J_d$  than the initial  $M_d$ , as predicted by the self-similar solutions, but it still does not affect the late time disk radius (see eq. [B7]). We do not plot our results for different  $\alpha$  since they are generally consistent with the analytic scalings above and in Appendix B.

## 4.2 Composition

The composition of the disk is important for determining the observational effects of any outflows. To this end, we plot the composition of our  $M_{d,0} = 0.3 M_{\odot}$ ,  $J_{49} = 2$  disk as a function of time in the upper panel of Figure 8. In the bottom panel we plot the relevant timescales for setting

<sup>5</sup> See Appendix B3 for the definition of  $p$ .

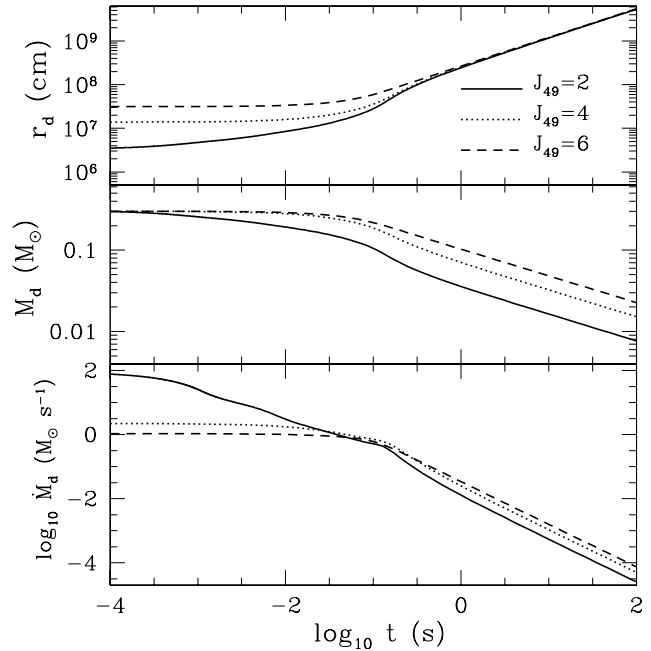


**Figure 7.** Similar to Fig. 1, but now taking the angular momentum to be  $J_{49} = 2$  (solid lines), 4 (dotted lines), and 6 (dashed lines). All solutions take  $M_{d,0} = 0.3 M_{\odot}$  with all other variables the same as in Fig. 1.

the composition, namely the viscous timescale,  $t_{\text{visc}}$  (solid line), the neutronization timescale  $t_n = 1/r_{e-p}$  (dotted line), and the timescale for  $\alpha$ -particle photodisintegration,  $t_{\text{photo}}$  (dashed line). At early times  $t_n \ll t_{\text{visc}}$ , so that an equilibrium value of  $Y_e \simeq 0.23$  is reached almost immediately. As the disk leaves the optically thick phase and becomes thinner, degeneracy pressure plays a larger role. This enhances neutron production, with a minimum  $Y_e \simeq 0.05$ . As the neutrino cooling subsides and the disk becomes thick again,  $Y_e$  increases. Before  $Y_e$  can reach  $\simeq 0.5$ , it freezes-out at a value of  $Y_e \simeq 0.3$  once  $t_n > t_{\text{visc}}$ .

Besides the neutron abundance, Figure 8 also highlights the production of  $\alpha$ -particles. Initially, the reactions needed to convert neutrons and protons to helium as well as photodisintegration of helium all happen on timescales much shorter than the disk evolution timescale (as an example, we plot the helium photodisintegration timescale in the bottom panel of Fig. 8), so that we can estimate the  $\alpha$ -particle mass fraction using chemical balance (eq. [17]). Once the  $\alpha$ -particle photodisintegration timescale becomes sufficiently long ( $t_{\text{visc}} < t_{\text{photo}}$ ), chemical equilibrium no longer applies and  $X_p = 0$ ,  $X_n = 1 - 2Y_e \simeq 0.4$ , and  $X_\alpha = 2Y_e \simeq 0.6$ .

Figure 9 shows how the late-time, frozen-out value of  $Y_e$  in the disk depends on the initial disk mass  $M_{d,0}$  and radius  $r_{d,0}$ , for two different initial electron fractions,  $Y_{e,0} = 0.1$  and  $Y_{e,0} = 0.5$ . The former is relevant for the disks created from NS-NS or BH-NS mergers (the focus of this paper), while a larger  $Y_{e,0} \simeq 0.5$  is appropriate for disks created during the accretion-induced collapse of a white-dwarf to a neutron star (e.g., Woosley & Baron 1992; Dessart et al. 2006). Figure 9 shows that for sufficiently compact disks, the disk reaches a modestly neutron-rich composition, with  $Y_e \simeq 0.3 - 0.4$ , independent of the initial composition.

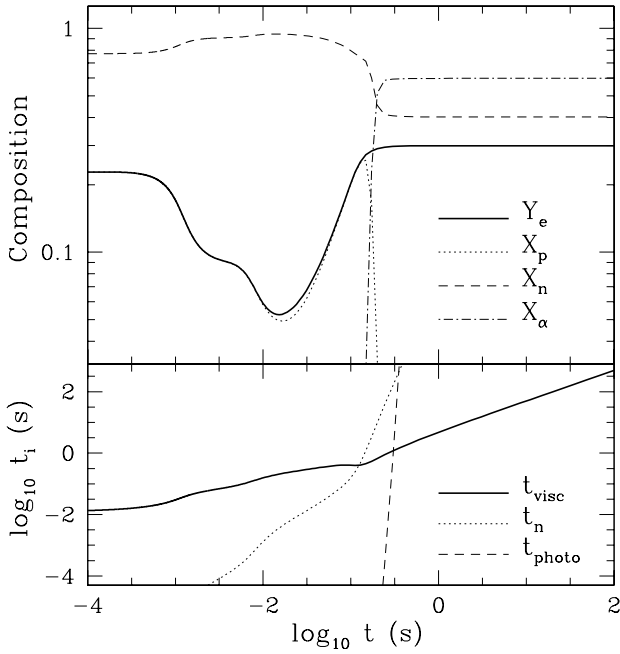


**Figure 8.** The composition and important reaction timescales as a function of time, for the  $M_{d,0} = 0.3M_\odot$  model from Fig. 1. In the top panel we plot the electron fraction,  $Y_e$  and the mass fraction of protons, neutrons, and  $\alpha$ -particles (see inset key). In the bottom panel we show the viscous time,  $t_{\text{visc}}$  (thick, solid line), the neutronization time,  $t_n = 1/r_{e-p}$  (dotted line), and the  $\alpha$ -particle photodisintegration time,  $t_{\text{photo}}$  (dashed line).

This is because, as highlighted in Figure 8, the timescale to come into  $\beta$ -equilibrium is shorter than the viscous time. For disks with a small initial mass and/or a large initial radius (the lower right-hand corner of each panel),  $t_n > t_{\text{visc}}$  and the disk retains its initial composition (set by the tidally-disrupted progenitor and the subsequent dynamical stage of the merger). Finally, neutrino irradiation of the outer disk by the inner disk can increase the freeze-out electron fraction, but we estimate this changes the freeze-out value of  $Y_e$  by at most  $\sim 20\%$ .<sup>6</sup>

## 5 DISK WINDS

Having described the evolution of the accretion disk as a function of time, we now discuss the properties of outflows from these hyper-accreting disks. Winds driven from deep within the BH potential well could produce relativistic jets and power late-time central engine activity. Outflows driven from larger radii dominate the system’s mass loss and may power supernova-like optical transients through the decay of radioactive isotopes that are synthesized in the wind (Li & Paczyński 1998; Kulkarni 2005). In both cases, the mass loss

<sup>6</sup> Our calculations employ the pair-capture cooling prescription of DiMatteo et al. (2002), which assume  $Y_e = 0.5$  and ultra-relativistic electrons; we find, however, that including the effects of degeneracy and arbitrary electron energies on the cooling changes the asymptotic electron fraction by at most a few percent.

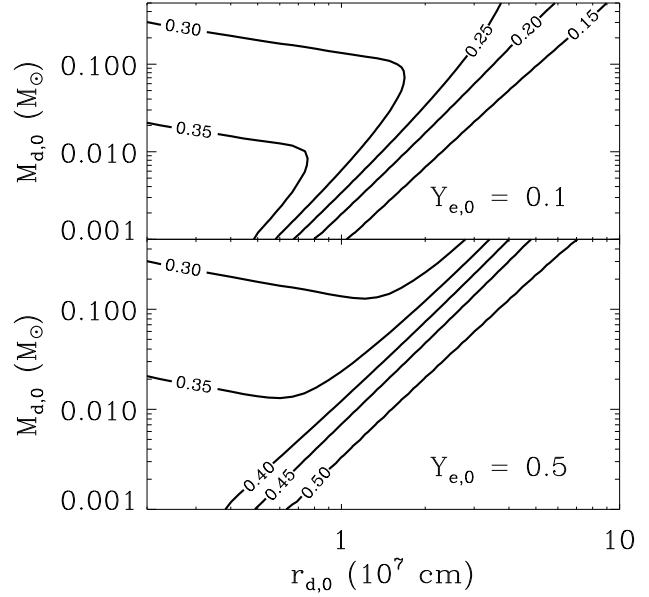


**Figure 9.** Contours of late-time electron fraction in the expanding disk as a function of initial disk mass  $M_{d,0}$  and radius  $r_{d,0}$ , for two different initial compositions. Relatively compact disks come into  $\beta$ -equilibrium and reach an electron fraction independent of the initial  $Y_e$ , while low mass, more extended disks retain their initial composition. Figure 8 shows the evolution of  $Y_e$  with time for one particular disk solution.

rate and nuclear composition are critical for determining the observable signature.

The type and character of the outflow depends on the disk’s thermodynamic state and changes as it passes through the different stages of evolution described in the previous section. In §5.1 we discuss early times when winds are due to neutrino irradiation of the thin, efficiently neutrino-cooled portions of the disk. We then consider thermally driven winds during thick, radiatively-inefficient accretion in §5.2. This dominates the mass loss at late times and blows away most of the remaining disk. In §5.3 we summarize the nuclear composition of the outflows during each phase. We predict an ejected  $^{56}\text{Ni}$  mass of at most  $\sim 10^{-3}M_\odot$  (§5.4). Its decay may power transient emission detectable following some short GRBs.

### 5.1 Neutrino-Heated Thin-Disk Winds

A wind with a mass loss rate  $\dot{M}_w$  driven from a thin disk at radius  $r$  must absorb a net power greater than  $\dot{E}_b = GM\dot{M}_w/2r$  to become unbound from the central BH. In principle,  $\dot{E}_b$  may be supplied by dissipation of the turbulence that produces the accretion shear stresses. “Viscous” heating of this kind only efficiently drives an outflow if a substantial fraction of the accretion power is dissipated in the disk’s upper atmosphere, where the cooling timescale is long compared to the wind’s outward advection timescale. However, local radiation MHD simulations to date suggest that very little energy dissipation occurs in the corona (e.g., Krolik et al. 2007). Instead, heating in the atmosphere above a thin, neutrino-cooled disk is likely dominated by neutrino irradiation. We therefore focus on



the neutrino-driven mass loss rate, which sets a *minimum*  $\dot{M}_w$ , and which can be reliably estimated. Neutrino-driven outflows from hyper-accreting disks have also been studied by Daigne & Mochkovitch (2002), Levinson (2006), Metzger et al. (2008a), and Barzilai & Levinson (2008); Dessart et al. (2008b) calculate the neutrino-driven mass loss from the central NS following a NS-NS merger under the assumption that collapse to a BH is not prompt.

The neutrino-driven mass loss rate is calculated by equating  $\dot{E}_b$  to the total neutrino heating rate in the disk's atmosphere. For the radii and entropies that characterize the winds, heating via electron neutrino absorption on baryons ( $p + \bar{\nu}_e \rightarrow n + e^+$  and  $n + \nu_e \rightarrow p + e^-$ ) dominates other forms of neutrino heating (e.g.,  $\nu - \nu$  annihilation and  $\nu - e^-$  scattering; see Qian & Woosley 1996; hereafter QW96). Since the neutrino absorption cross section,  $\sigma_{\nu N} \simeq 5 \times 10^{-44} \langle \epsilon_\nu^2 \rangle$  MeV $^{-2}$  cm $^2$ , increases with neutrino energy, neutrinos radiated from near the inner radius  $r_*$  dominate. Assuming that the  $\nu_e$  and  $\bar{\nu}_e$  luminosities and spectra are approximately equal and can be approximated as originating from a point source at small radii, the neutrino heating rate through a surface density  $\Sigma$  at radius  $r$  is

$$q_\nu^+ = \frac{L_\nu \sigma_{\nu N} \Sigma}{4\pi m_N r^2} \simeq 2 \times 10^{39} L_{52} \langle \epsilon_{10}^2 \rangle \Sigma_{18} r_6^{-2} \text{ ergs s}^{-1} \text{ cm}^{-2}, \quad (22)$$

where  $r = 10^6 r_6$  cm,  $L_\nu = 10^{52} L_{52}$  ergs s $^{-1}$ ,  $\langle \epsilon_\nu^2 \rangle = 100 \langle \epsilon_{10}^2 \rangle$  MeV $^2$ , and  $\Sigma = \Sigma_{18} 10^{18}$  g cm $^{-2}$ . This expression assumes that the absorbing layer is optically thin, i.e., that  $\tau_\nu \equiv \Sigma \sigma_{\nu N} / m_N \simeq 3 \Sigma_{18} \langle \epsilon_{10}^2 \rangle < 1$ .

First, consider neutrino heating in comparison to viscous heating in the midplane. This ratio is largest when the disk is marginally optically thick ( $\tau_\nu \simeq 1$ ), peaking at a value of

$$\frac{q_\nu^+}{q_{\text{visc}}} \Big|_{\tau_\nu \simeq 1} \simeq 0.5 \left( \frac{\epsilon}{0.1} \right) \left( \frac{f}{1.6} \right) \left( \frac{A}{3.6} \right)^{3/5} \langle \epsilon_{10}^2 \rangle^{2/5} J_{49}^{2/5} M_3^{-6/5}, \quad (23)$$

where  $\epsilon \equiv L_\nu / \dot{M}_d c^2$  is the disk's radiative efficiency. Thus, although we neglected neutrino heating in §4, it may become somewhat important when  $\tau_\nu \sim 1$  and should be included in a more detailed calculation.

We now consider a wind that emerges from the disk in the  $z$ -direction, parallel to the rotation axis. Away from the disk midplane, neutrino heating dominates over viscous heating, balancing cooling ( $q_\nu^+ = q_\nu^-$ ) at a slightly lower temperature,  $T_\nu \simeq 3.3 L_{52}^{1/6} \langle \epsilon_{10}^2 \rangle^{1/6} r_6^{-1/3}$  MeV. Moving further out in the hydrostatic atmosphere, the temperature slowly decreases below  $T_\nu$ . Due to the strong temperature dependence of the pair capture cooling rate ( $q_\nu^- \propto T^6$ ), a “gain region” of net neutrino heating (i.e.,  $q_\nu^+ > q_\nu^-$ ) develops above a height  $z_{\text{gain}}$ . This net heating drives an outflow.

The thermal power deposited in the upper disk atmosphere  $\dot{E}_\nu$  is the specific heating rate  $q_\nu^+ / \Sigma$  (eq. [22]) multiplied by the mass of the atmosphere in the gain region  $M_{\text{gain}} \simeq 2\pi H(z_{\text{gain}}) r^2 \rho(z_{\text{gain}})$ , where  $H(z_{\text{gain}})$  is the scale height near the base of the gain region. Although the midplane of a neutrino-cooled disk is generally dominated by nonrelativistic gas pressure (see Fig. 5), the gain region has a sufficiently low density that it is instead dominated by radiation pressure  $P_{\text{rad}} = (11/12) a T^4$ . Its scale height is

$H(z_{\text{gain}}) \simeq (P_{\text{rad}} / \rho g_z)|_{z_{\text{gain}}}$ , where  $g_z$  is the gravitational acceleration in the  $z$ -direction. Since  $H(z_{\text{gain}})$  is less than the midplane scale height  $H$ ,  $z_{\text{gain}} \simeq H$  and  $g_z \simeq GMH/r^3$ . The atmosphere in the gain region is roughly isothermal so we set  $T(z_{\text{gain}}) \approx T_\nu$ . By combining these estimates and equating  $\dot{E}_\nu$  with  $\dot{E}_b$  we find that the neutrino-driven mass loss rate from a thin disk is

$$\dot{M}_\nu|_{S^a \gg S_N} \approx 10^{-6} L_{52}^{5/3} \langle \epsilon_{10}^2 \rangle^{5/3} r_6^{5/3} M_3^{-2} (H/r)^{-1} M_\odot \text{s}^{-1}, \quad (24)$$

analogous to that derived by QW96 for proto-neutron star winds. The assumption that the atmosphere is radiation dominated is only valid if the asymptotic entropy in relativistic particles  $S^a$  exceeds that in nonrelativistic nucleons  $S_N \simeq 6 + \ln(T_{\text{MeV}}^3 / \rho_{10}) k_B$  baryon $^{-1}$ , where  $T = T_{\text{MeV}}$  MeV. By dividing the energy gained by a nucleon in the wind  $\simeq GMm_N/2r$  by the gain region temperature  $T(z_{\text{gain}})$ , we estimate

$$S^a \simeq 60 L_{52}^{-1/6} \langle \epsilon_{10}^2 \rangle^{-1/6} r_6^{-2/3} M_3 k_B \text{ baryon}^{-1} \quad (25)$$

as the asymptotic wind entropy.

Although equation (24) does not strictly hold when  $S^a \sim S_N$ , QW96 show that  $\dot{M}_\nu$  scales the same way with  $L_\nu$ ,  $\langle \epsilon_\nu^2 \rangle$ ,  $M$ , and  $r$ , but with a larger normalization of

$$\dot{M}_\nu|_{S^a \sim S_N} \approx 10^{-5} L_{52}^{5/3} \langle \epsilon_{10}^2 \rangle^{5/3} r_6^{5/3} M_3^{-2} (H/r)^{-1} M_\odot \text{s}^{-1}. \quad (26)$$

The mass loss rate is higher for low entropy winds because neutrino heating peaks further off the disk surface, which reduces the binding energy and gravitational acceleration of matter in the gain region. Using the numerical disk wind calculations described in Metzger et al. (2008b; hereafter M08b) we have verified that equation (26) holds to within a factor  $\simeq 2$  when  $S^a \sim S_N$ .

In deriving equations (24) and (26), we have implicitly assumed that the timescale for neutrinos to heat matter in the gain region  $t_{\text{heat}} \equiv (U_{\text{th}} \Sigma / \rho q_\nu^+) |_{z_{\text{gain}}}$ , where  $U_{\text{th}} \simeq 3P_{\text{rad}}$  is the thermal energy density, is short compared to  $t_{\text{visc}}$ , the timescale over which the disk properties appreciably change. Equating  $S^a$  (eq. [25]) to the entropy in relativistic particles  $\propto T^3 / \rho$ , we find that

$$\rho(z_{\text{gain}}) \simeq 10^8 r_6^{-1/3} L_{52}^{2/3} \langle \epsilon_{10}^2 \rangle^{2/3} M_3^{-1} \text{ g cm}^{-3}. \quad (27)$$

Then, using equations (22) and (27), we have that<sup>7</sup>

$$t_{\text{heat}} \simeq \frac{3P_{\text{rad}}}{\rho(q_\nu^+ / \Sigma)} \Big|_{z_{\text{gain}}} \simeq 0.1 \text{ s } L_{52}^{-1} r_6 \langle \epsilon_{10}^2 \rangle^{-1} M_3 \quad (28)$$

For most of the disk solutions considered in this paper, we find that  $t_{\text{heat}} \lesssim t_{\text{visc}}$  during the thin disk phase; thus, equations (24) and (26) are reasonably applicable near  $r_d$ .

Figure 10 compares the accretion rate  $\dot{M}_d$  (*solid line*) with the neutrino-driven mass loss rate  $\dot{M}_\nu$ . In order to determine  $L_\nu$  and  $\langle \epsilon_\nu^2 \rangle$ , we calculated steady-state disk models (e.g., DiMatteo et al. 2002) with the accretion rate set at each time according to our ring model with  $J_{49} = 2$  and  $\dot{M}_d = 0.3 M_\odot$ . We plot the neutrino-driven mass loss rate  $\dot{M}_\nu$  (eqs. [24] and [26]) at small (*dotted line*) and large (*short-dashed line*) radii. This shows that the mass loss is dominated by large radii where the majority of the mass lies,

<sup>7</sup> Equation (28) is also approximately equal to the outward advection timescale of the wind in the heating region.

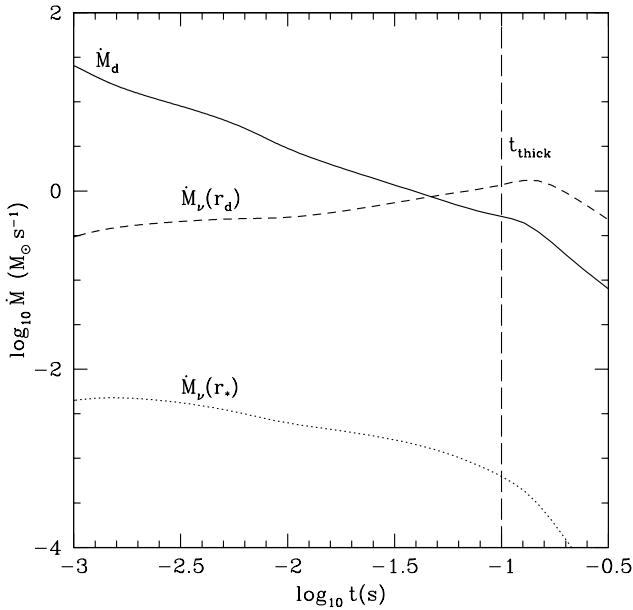


**Figure 10.** The accretion rate  $\dot{M}_d$  (solid line) and neutrino-driven mass loss rates  $\dot{M}_\nu$  for our  $J_{49} = 2$  and  $M_{d,0} = 0.3M_\odot$  model, focusing on the phase of thin, efficiently neutrino-cooled accretion. The neutrino-driven mass loss rate  $\dot{M}_\nu$  (interpolated between eqs. [24] and [26]) is shown at the inner disk radius ( $r_* = 10^6$  cm; dotted line) and at the outer disk radius (near  $r_d$ , short-dashed line). The disk is advective to the right of the vertical line (eq. [20]), at which point the mass-loss will no longer be dominated by neutrino irradiation.

as expected since  $\dot{M}_\nu \propto r^{5/3}$ . The vertical dot-dashed line marks where the disk transitions to being thick (eq. [20]), after which neutrino-heating no longer dominates the wind mass loss.

Outflows that are launched from small radii, near  $r_*$ , have the greatest potential to produce relativistic jets and to power high energy emission. But as we now argue, these neutrino-driven winds are too massive to become highly relativistic. Our calculation above focused on purely thermal, neutrino-driven winds, which accelerate matter to only a fraction of the escape speed (and thus are mildly relativistic). However, in the presence of a strong, large scale open poloidal magnetic field, a more powerful, magnetically-driven outflow is possible. Magnetocentrifugal support in the wind’s hydrostatic atmosphere may further enhance mass loss (e.g., Levinson 2006), but equation (24) still represents the *minimum* mass loading on field lines which thread a neutrino-cooled disk. Figure 10 shows that  $\dot{M}_\nu(r_*) \sim 10^{-4} - 10^{-2} M_\odot \text{ s}^{-1}$  during the thin disk phase. The luminosities of the prompt emission and late-time X-ray flares from short GRBs, however, do not typically exceed  $L_\gamma \sim 10^{50} \text{ erg s}^{-1}$  (and are often much lower; Nakar 2007). Thus, even assuming a modest radiative efficiency for the outflow of  $\epsilon_w \sim 0.1$ , the Lorentz factor  $\Gamma$  of a neutrino-heated disk wind must obey  $\Gamma \simeq L_\gamma / [\epsilon_w \dot{M}_\nu(r_*) c^2] \lesssim 5$ , which is inconsistent with existing compactness constraints on short GRBs (Nakar 2007). A more likely source for the relativistic outflows that power short GRBs and their late-time flares are nearly baryon-free field lines which thread the BH’s event

horizon (e.g., McKinney 2005). In addition, in §5.2 we argue that when the disk becomes advection dominated and neutrino irradiation effectively ceases, jet production may be more likely.

## 5.2 Radiatively-Inefficient Thick Disk Winds

At late times ( $t \sim t_{\text{thick}}$ ; eq. [20]) the disk transitions from thin and neutrino-cooled to being advective. At this point a neutrino-driven outflow is unlikely to dominate the mass loss, in part because the neutrino luminosity precipitously drops (Fig. 3 & 4). In addition, because RIAFs possess a positive Bernoulli parameter, a powerful viscously-driven outflow is likely (Blandford & Begelman 1999; Stone & Pringle 2001; Proga & Begelman 2003).

In §4.1 we showed that the disk becomes radiatively inefficient external to an “ignition radius”  $r_{\text{ign}} \propto \dot{M}_d^{6/5}$  (eq. [19]). The outer disk, near  $r_d$ , thickens first (when  $r_d \sim r_{\text{ign}}$  at  $t \sim t_{\text{thick}}$ ) and radiatively inefficient conditions move inwards as  $\dot{M}_d$  decreases. In the simplest picture, one might expect that the innermost radii become an RIAF only once  $\dot{M}_d$  drops from its value at  $t \sim t_{\text{thick}}$  by an additional factor  $\sim (r_*/r_d)^{5/6}$ . In fact, the *entire* disk probably become radiatively inefficient on a timescale similar to  $t_{\text{thick}}$  if the accretion rate which reaches small radii abruptly decreases once the outer disk thickens (Fig. 6). Hence, at a time  $t_{\text{thick}}$ , a significant portion of the accreting matter may be redirected into an outflow, with only a fraction  $\sim (r_*/r_d)$  reaching small radii and accreting onto the BH (Stone & Pringle 2001).

X-ray binaries typically produce radio jets upon transitioning from their “high-soft” (radiatively efficient) to “low-hard” (radiatively inefficient) states (e.g., Remillard & McClintock 2006). In analogy, once the inner disk becomes an RIAF, conditions seem to favor the production of relativistic jets (see also Lazzati et al. 2008).<sup>8</sup>

Even if only a fraction  $(r_*/r_d)$  of the mass remaining when the disk thickens actually reaches the origin, the total energy supply available would be

$$\begin{aligned}
 E_{\text{jet}} &\equiv \epsilon_{\text{jet}} \dot{M}_d(t_{\text{thick}}) c^2 \left( \frac{r_*}{r_d(t_{\text{thick}})} \right) \\
 &\simeq 3 \times 10^{50} \left( \frac{\epsilon_{\text{jet}}}{0.1} \right) \left( \frac{r_*}{10^6 \text{ cm}} \right) \alpha_{0.1}^{6/17} M_3^{-4/17} \left( \frac{J_{49}}{2} \right)^{8/17} \text{ ergs},
 \end{aligned}
 \tag{29}$$

where  $\epsilon_{\text{jet}}$  is the fraction of the accretion energy used to power a jet and we have estimated  $\dot{M}_d(t_{\text{thick}})$  and  $r_d(t_{\text{thick}})$  using the self-similar thick disk solutions (eqs. [B5] and [B7], respectively). Equation (29) shows that the accretion energy available from near  $r_*$  following the RIAF transition is more than sufficient to power the late-time X-ray flares observed following some short GRBs. If this is the case,  $t_{\text{thick}}$  sets a characteristic timescale for late-time central engine activity. If  $\alpha \lesssim 10^{-3}$ ,  $t_{\text{thick}}$  may be large enough to explain the  $\sim 30$  s delay until flaring observed for some short GRBs (e.g., Berger et al. 2005; Villasenor et al. 2005). However, very late time energy injection, such as the *Chandra* flare observed

<sup>8</sup> This is in stark contrast to jets powered by neutrino annihilation along the polar axis, which require a *high* radiative efficiency.

two weeks after GRB050709 (Fox et al. 2005), appears to require an alternative explanation. In addition, given observational evidence for  $\alpha \sim 0.1$  in a number of environments (King et al. 2007), it may be more natural to associate  $E_{\text{jet}}$  and  $t_{\text{thick}}$  with the energy and duration, respectively, of the short GRB itself, rather than the late-time central engine activity (see §6).

### 5.3 Outflow Nuclear Composition

The outflow nuclear composition has important consequences for the observable signature of compact object mergers. Nonrelativistic outflows are sufficiently dense to synthesize heavy isotopes (Pruet et al. 2004; Surman et al. 2006), which may power transient emission via radioactive decay. The isotopic yield depends on the speed, thermodynamic properties, and the asymptotic electron fraction  $Y_e^a$  in the outflow.<sup>9</sup> Although relativistic winds from the inner disk are unlikely to synthesize anything heavier than He (Lemoine 2002; Beloborodov 2003a),  $Y_e^a$  is important in this case as well. A neutron-rich outflow may alter the jet’s dynamics and the prompt and afterglow emission from that of the standard GRB fireball model (e.g., Derishev et al. 1999; Beloborodov 2003b; Rossi et al. 2006).

Figure 11 delineates different regimes of outflow properties and composition (as given by  $Y_e^a$ ) as a function of the wind launching radius  $r$  and accretion rate  $\dot{M}_d$ . We fix  $\alpha = 0.1$  and  $M = 3M_\odot$ . The time-dependent evolution of the ring radius  $r_d$  is shown for a solution with  $J_{49} = 2$  and  $M_{d,0} = 0.3M_\odot$  (solid line). At each time a given steady-state disk profile can be read off of this plot as a horizontal line that extends from the far left and ends on  $r_d$ . Therefore, outflows from radii interior to  $r_d$  contribute to the disk’s total nucleosynthetic yield.

The ignition radius  $r_{\text{ign}}$  (eq. [19]) is shown in Figure 11 with a short dashed line. For  $r \gtrsim r_{\text{ign}}$  the disk is an RIAF and marked in the figure as “Thick Disk.” In this case, a viscously driven outflow dominates (§5.2). Since outflows from RIAFs escape the disk in roughly the accretion timescale, these winds retain the midplane electron fraction (M08b), so that  $Y_e^a \simeq Y_e^{\text{mid}} \ll 0.5$  (because the disk itself freezes-out neutron-rich, as summarized in §4.2 and Fig. 9).

For  $r \lesssim r_{\text{ign}}$ , the disk is efficiently neutrino-cooled and marked in Figure 11 as “Thin Disk.” The absorption of neutrinos, which heats the outflow and unbinds it from the BH may also alter its nucleonic composition. This drives  $Y_e^a$  to a value set by the neutrino radiation field  $Y_e^\nu$ , which in general is different from  $Y_e^{\text{mid}}$ . A simple criterion was discussed by M08b for determining when  $Y_e^a \simeq Y_e^\nu$ . A typical nucleon in the accretion disk at radius  $r$  must absorb an energy  $\simeq GMm_N/2r$  to become unbound from the BH, so that  $N_\nu \simeq GMm_N/2r\langle\epsilon_\nu\rangle$  neutrinos must be absorbed per nucleon. If we take  $N_\nu > Q \sim 2 - 3$ , then a typical nucleon has changed its identity ( $p \rightarrow n$  or  $n \rightarrow p$ ) at least several times.

This implies that all purely neutrino-driven outflows from radii smaller than

<sup>9</sup> The *asymptotic* electron fraction is germane because heavy nuclei primarily form after freeze-out from  $\beta$ -equilibrium.

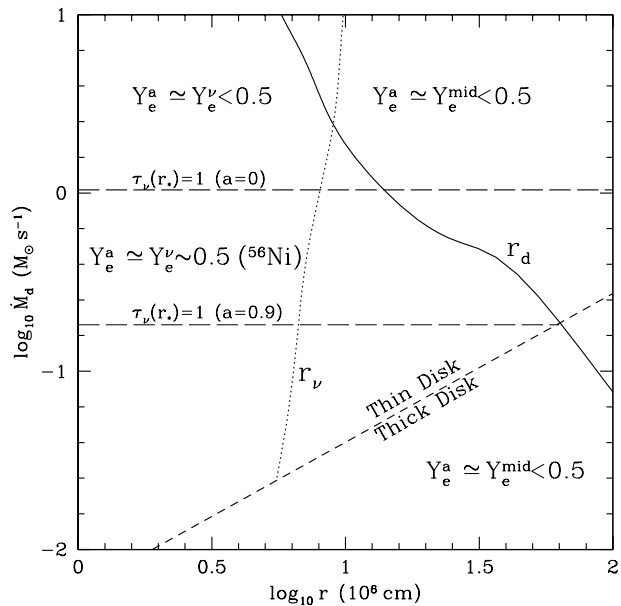


**Figure 11.** Asymptotic electron fraction  $Y_e^a$  for disk winds as a function of the wind launching radius  $r$  and accretion rate  $\dot{M}_d$  (for  $\alpha = 0.1$  and  $M = 3M_\odot$ ). The solid line indicates the location of the ring radius  $r_d$  for our fiducial solution with  $M_{d,0} = 0.3M_\odot$  and  $J_{49} = 2$ . The short dashed line is the “ignition” radius  $r_{\text{ign}}$  (eq. [19]). Exterior to this (marked “Thick Disk”) the disk is advective with a viscously driven wind of composition  $Y_e^a \simeq Y_e^{\text{mid}} < 0.5$ . Interior to  $r_{\text{ign}}$  (marked “Thin Disk”) a neutrino-driven wind occurs. The dotted line shows  $r = r_\nu$  with  $Q = 2$  (eq. [30]) and determines where the neutrino absorptions necessary to unbind matter alter the wind composition, so that  $Y_e^a \simeq Y_e^{\text{mid}} < 0.5$  ( $Y_e^a \simeq Y_e^\nu$ ) exterior (interior) to  $r_\nu$ . The  $\dot{M}_d$  above which  $\tau(r_*) > 1$  is plotted for BH spins of  $a = 0$  and  $a = 0.9$ . Above this line, the  $\bar{\nu}_e$  and  $\nu_e$  spectra differ and  $Y_e^\nu < 0.5$ , while below this their spectra are similar and  $Y_e^\nu \simeq 0.5$ . In the region where  $r < r_{\text{ign}}$ ,  $\tau_\nu(r_*) < 1$ , and  $r < r_\nu$  (i.e., the middle/lower left-hand trapezoid),  $Y_e^a \simeq Y_e^\nu \sim 0.5$ ; these conditions are favorable for  $^{56}\text{Ni}$  production (see §5.4).

$$r_\nu \equiv \frac{GMm_p}{2Q\langle\epsilon_\nu\rangle} \simeq 10^7 M_3 \langle\epsilon_{10}\rangle^{-1} (Q/2)^{-1} \text{ cm}, \quad (30)$$

where  $\langle\epsilon_\nu\rangle \equiv 10\langle\epsilon_{10}\rangle$  MeV, achieve  $Y_e^a \simeq Y_e^\nu$ , independent of the disk’s midplane composition.

We plot  $r_\nu$  with  $Q = 2$  as a dotted line in Figure 11, where  $\langle\epsilon_\nu\rangle$  is calculated from  $\dot{M}_d$  using our steady-state disk solutions (see §5.1). For  $r \lesssim r_\nu$ , any neutrino-driven outflow enters equilibrium with the neutrino radiation field (i.e.,  $Y_e^a \simeq Y_e^\nu$ ). For  $r \gtrsim r_\nu$  the outflow approximately retains the midplane electron fraction (i.e.,  $Y_e^a \simeq Y_e^{\text{mid}}$ ).

Although we have established the conditions under which  $Y_e^a$  is determined by neutrino absorptions, we must now address what sets  $Y_e^\nu$  itself. If the rate of neutrino absorptions exceeds the rate of degenerate pair captures before the wind falls out of  $\beta$ -equilibrium,  $Y_e^\nu$  is

$$Y_e^\nu \equiv \left( 1 + \frac{L_{\bar{\nu}_e} \langle\epsilon_{\bar{\nu}_e}\rangle - 2\Delta + 1.2\Delta^2 / \langle\epsilon_{\bar{\nu}_e}\rangle}{L_{\nu_e} \langle\epsilon_{\nu_e}\rangle + 2\Delta + 1.2\Delta^2 / \langle\epsilon_{\nu_e}\rangle} \right)^{-1}, \quad (31)$$

where  $\Delta = 1.293$  MeV is the neutron-proton mass difference, and  $L_{\nu_e}/L_{\bar{\nu}_e}$  and  $\langle\epsilon_{\nu_e}\rangle/\langle\epsilon_{\bar{\nu}_e}\rangle$  are the mean  $\nu_e/\bar{\nu}_e$  luminosities and energies, respectively, from a centrally-concentrated

source (Qian et al. 1993; QW96). Equation (31) demonstrates that the  $\nu_e$  and  $\bar{\nu}_e$  spectra are crucial for setting  $Y_e^\nu$ .

Since the disk's luminosity and temperature peak at just a few  $r_g$ ,  $Y_e^\nu$  is primarily determined by conditions at small radii. At early times, the accretion disk may be optically thick near  $r_*$  and so the  $\nu_e$  and  $\bar{\nu}_e$  spectra depend on the temperatures at  $\nu_e$  and  $\bar{\nu}_e$  neutrinospheres, respectively. Since there are more neutrons than protons in the disk, the optical depth to  $\nu_e$  through the disk is higher than to  $\bar{\nu}_e$ ; thus, the temperature at the  $\bar{\nu}_e$  neutrinosphere is higher than at the  $\nu_e$  neutrinosphere. This implies  $L_{\bar{\nu}_e} \gg L_{\nu_e}$ ,  $\langle \epsilon_{\bar{\nu}_e} \rangle \gg \langle \epsilon_{\nu_e} \rangle$ , and thus  $Y_e^\nu \ll 0.5$ . Using 3-dimensional calculations of the merger of NSs with zero spin, Rosswog & Liebendörfer (2003) find that at  $\sim 15$  ms following merger,  $L_{\bar{\nu}_e} \simeq 3.5L_{\nu_e}$ ,  $\langle \epsilon_{\nu_e} \rangle \simeq 9$  MeV, and  $\langle \epsilon_{\bar{\nu}_e} \rangle \simeq 15$  MeV, which implies  $Y_e^\nu \simeq 0.21$ , consistent with our arguments (see also Surman et al. 2008). We conclude that when the disk is optically-thick near  $r_*$ , a neutron-rich outflow is again the most likely outcome. The critical accretion rate at which  $\tau_\nu(r_*) = 1$  is shown in Figure 11 with a long dashed line for both  $a = 0$  and  $a = 0.9$ .

Once the disk becomes optically thin near  $r_*$ , the difference between the  $\nu_e$  and  $\bar{\nu}_e$  spectra is much less pronounced. This occurs because (1) the neutrinos and antineutrinos originate from regions with the same temperature; (2) any net lepton flux out of the disk must remain modest (i.e.,  $L_{\nu_e}/\langle \epsilon_{\nu_e} \rangle \simeq L_{\bar{\nu}_e}/\langle \epsilon_{\bar{\nu}_e} \rangle$ ); and (3) the difference between the  $e^-$  and  $e^+$  capture cross sections for  $kT \gg \Delta - m_e c^2$  is small. Taking  $\langle \epsilon_{\nu_e} \rangle \sim \langle \epsilon_{\bar{\nu}_e} \rangle \gg \Delta$ , equation (31) shows that  $Y_e^\nu \simeq 0.5$ , a value in the range required to produce  $^{56}\text{Ni}$  (which we discuss further in §5.4). Indeed, M08b used the steady-state, optically-thin  $\alpha$ -disk calculations of Chen & Beloborodov (2007; hereafter CB07) to calculate the neutrino radiation fields carefully, and showed that  $Y_e^\nu \gtrsim 0.5$  over the majority of the disk (see their Fig. 1). Although the precise spectra extracted from an  $\alpha$ -disk calculation should be taken with caution, the conclusion that the  $\nu_e$  and  $\bar{\nu}_e$  spectra are similar for optically thin accretion (and  $Y_e^\nu \simeq 0.5$ ) is probably robust.

Figure 11 illustrates that under most conditions the outflows from hyper-accreting disks are neutron-rich. Neutron-rich material ejected during the initial dynamical phase of compact object mergers has long been considered a promising source for producing Galactic  $r$ -process elements, whose precise astrophysical origin remains uncertain (Lattimer & Schramm 1974; see, however, Qian 2000). In addition, Surman et al. (2008) find that winds driven from the remnant accretion disk at early times (when it is optically thick; upper left quadrant of Fig. 11) are sufficiently neutron-rich to produce successful  $r$ -process. The outflows driven from the advective disk at late times, however, are unlikely to produce  $r$ -process elements, given their modest entropies and electron fractions of  $Y_e \gtrsim 0.3$  (Figs. 8 and 9). Instead, this modest  $Y_e$  material will be synthesized to form intermediate mass neutron rich isotopes (Hartmann et al. 1985).

#### 5.4 $^{56}\text{Ni}$ Production and Optical Transients

As summarized in Figure 11, most of the material in the outflow driven from a hyper-accreting disk will be neutron-rich. Nonrelativistic neutron-rich ejecta are difficult to detect be-

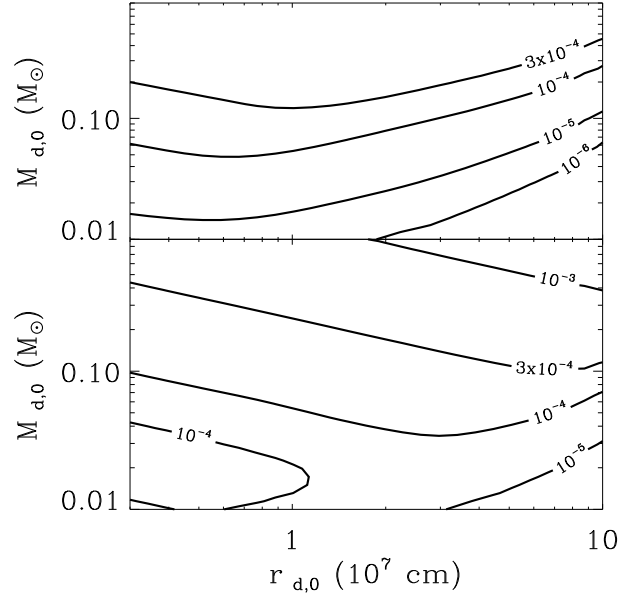


**Figure 12.** Contours of total  $^{56}\text{Ni}$  mass  $M_{\text{Ni}} \equiv (X_{\text{Ni}}/0.4)M_{Y_e=0.5}$  (in units of  $M_\odot$ ) produced in the neutrino-driven outflows as a function of the initial disk mass  $M_{d,0}$  and initial ring radius  $r_{d,0}$ , where  $M_{Y_e=0.5}$  is the total mass loss with  $Y_e^a \simeq 0.5$  (based on the arguments in Fig. 11) and  $X_{\text{Ni}}$  is the average  $^{56}\text{Ni}$  mass fraction synthesized in the wind. The upper and lower panels correspond to non-rotating ( $a = 0$ ) and rapidly spinning ( $a = 0.9$ ) BHs, respectively.

cause isotopes synthesized from low  $Y_e$  material are themselves very neutron-rich and typically possess very short half-lives, on the order of seconds (e.g., Freiburghaus et al. 1999). Thus, most of the radioactive energy is released at high optical depths and suffers severe adiabatic losses before the photons can diffusively escape. By contrast, ejecta with  $Y_e^a \simeq 0.5$  are easier to detect because they can produce a significant quantity of  $^{56}\text{Ni}$  (Hartmann et al. 1985), an isotope better suited to powering observable emission because its half-life  $\simeq 6$  days is comparable to the timescale on which the outflow becomes optically thin. From Figure 11 we see that outflows in a modest range of parameter space (middle/lower-left trapezoid) are capable of synthesizing  $^{56}\text{Ni}$ . One caveat to this conclusion is that it only applies if the winds are primarily neutrino driven. If the outflow is instead magnetocentrifugally driven by a moderately strong open poloidal magnetic field (e.g., Levinson 2006; Xie et al. 2007), then  $Y_e^a \ll 0.5$  can result, even if  $Y_e^\nu \simeq 0.5$  (M08b). In what follows we assume that the wind's are primarily neutrino driven.

Under this assumption, Figure 12 shows the total  $^{56}\text{Ni}$  mass,  $M_{\text{Ni}} = (X_{\text{Ni}}/0.4)M_{Y_e=0.5}$ , produced in outflows from hyper-accreting disks as a function of the disk's initial mass  $M_{d,0}$  and radius  $r_{d,0}$ , where  $M_{Y_e=0.5}$  is the total mass loss with  $Y_e^a \simeq 0.5$  and  $X_{\text{Ni}}$  is the average  $^{56}\text{Ni}$  mass fraction synthesized in the wind. We calculate  $M_{Y_e=0.5}$  by integrating the neutrino-driven mass loss (eqs. [24] and [26]) across the  $Y_e^a \simeq 0.5$  region in Figure 11, using  $r_d(t)$  and  $\dot{M}_d(t)$  from the disk evolution calculations described in §4.

Pruet et al. (2004) present calculations of  $X_{\text{Ni}}$  which are parameterized in terms of the asymptotic entropy  $S^a$ ,

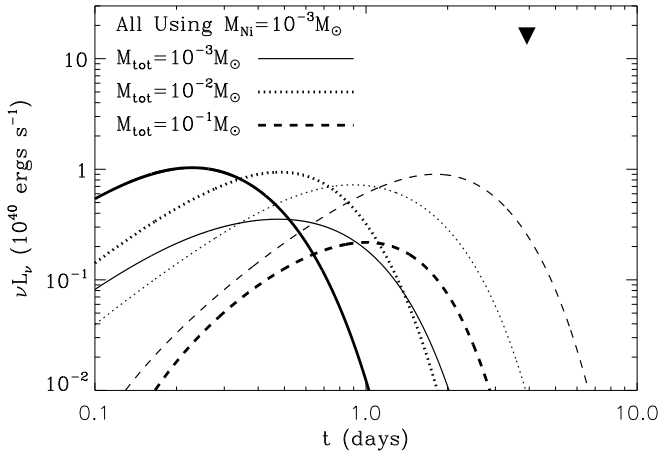


**Figure 13.** Luminosity of Ni decay-powered “macronovae” as a function of time since merger for Ni mass  $M_{\text{Ni}} = 10^{-3}M_{\odot}$  and ejecta velocity  $v^a = 0.1$  c. Light curves are shown for three values of the total ejected mass  $M_{\text{tot}} = 10^{-3}$  (solid line),  $10^{-2}$  (dotted line), and  $10^{-1}M_{\odot}$  (dashed line). The luminosities in V and J-Band (0.44 and 1.26  $\mu\text{m}$ , respectively) are shown with thick and thin lines, respectively. The V-band upper limit on emission following GRB050509B from Hjorth et al. (2005) is shown with a filled triangle.

mass loss rate  $\dot{M}_w$ , and asymptotic velocity  $v^a$  of an outflow with  $Y_e^a \simeq 0.51$ .  $M_{Y_e=0.5}$  is dominated by outflows from radii  $\sim 3 \times 10^6 - 10^7$  cm when  $\dot{M}_d \sim 0.1 - 1M_{\odot} \text{ s}^{-1}$  (corresponding to  $L_{52} \sim \text{few}$ ); equation (25) thus gives  $S^a \sim 10 - 30k_B \text{ baryon}^{-1}$  for the ejecta with  $Y_e^a \simeq 0.5$ . Purely neutrino-driven winds achieve asymptotic velocities which are typically below the escape speed of the central object (e.g., Thompson et al. 2001); thus, the asymptotic kinetic energy is most likely dominated by energy released during the formation of heavy elements. Because  $\sim 8$  MeV baryon $^{-1}$  is released in producing Fe-peak elements, we estimate that  $v^a \simeq 0.1 - 0.15$  c. Applying these wind parameters to Figure 3 of Pruet et al. (2004), we estimate that  $X_{\text{Ni}} \sim 0.2 - 0.5$ , thereby justifying our scaling for  $X_{\text{Ni}}$  in Figure 12.

Figure 12 shows that for large initial disk masses ( $M_{d,0} \gtrsim 0.1M_{\odot}$ ), the ejected Ni mass,  $\sim 3 \times 10^{-4} - 10^{-3}M_{\odot}$ , can be appreciable. Disks with moderate initial radii  $r_{d,0} \sim 10^7$  cm are optimal for producing  $^{56}\text{Ni}$  because they are sufficiently large to contain the radius  $r_{\nu} \sim 10^7$  cm and yet are sufficiently compact to have a large initial accretion rate, which maximizes the neutrino luminosity and thus the neutrino-driven mass loss. Conveniently, initial disk parameters from many compact object merger simulations (see §2) are in the range required to produce  $\sim 10^{-4} - 10^{-3}M_{\odot}$  of Ni.

The decay of  $M_{\text{Ni}} \sim 10^{-4} - 10^{-3}M_{\odot}$  can reheat the (adiabatically cooled) ejecta sufficiently to produce detectable transient emission. In order to explore this possibility, we calculate the light curves of ejecta heated by Ni decay (“macronovae”) using the method of Kulkarni (2005). This simplified one-zone model accounts for the fraction of the gamma-rays produced by the Ni decay which are absorbed by the expanding material (Colgate et al. 1980) and

assumes blackbody emission at the photosphere, neglecting Comptonization.

Figure 13 shows the V and J-band luminosities as a function of time since the merger for an outflow with Ni mass  $M_{\text{Ni}} = 10^{-3}M_{\odot}$  which is expanding at  $v^a = 0.1$  c. The V-band light curve peaks earlier because the temperature at the photosphere decreases as the material expands. Somewhat after the peak in the light curves, recombination will decrease the opacity well below that considered here; thus our calculations are not quantitatively reliable at these times. The total mass  $M_{\text{tot}}$  ejected during the merger event, most of it neutron rich, is likely to be significantly larger than  $M_{\text{Ni}}$ ; this provides additional opacity for the Ni-rich material. To explore the effect of this additional material on the detectability of the Ni decay, the light curves in Figure 13 are shown for three values of  $M_{\text{tot}}$ :  $10^{-3}M_{\odot}$  (solid line),  $10^{-2}M_{\odot}$  (dotted line), and  $10^{-1}M_{\odot}$  (dashed line). As Figure 13 shows, larger  $M_{\text{tot}}$ : (1) delays the time to peak emission ( $t_{\text{peak}}$  is roughly  $\propto M_{\text{tot}}^{1/2}$ ); (2) increases the total fluence of the event by trapping a higher fraction of the gamma-ray emission; and (3) increases the peak wavelength of the emission, pushing it into the near-IR for large  $M_{\text{tot}}$ . We conclude that long wavelength ( $\lambda \gtrsim \mu\text{m}$ ) observations at  $t \sim 1$  day are the most promising for the detection of a Ni decay-powered macronova.

Hjorth et al. (2005) place an upper limit of  $M_V > 27.5$  at  $t = 3.9$  days on any emission associated with the short GRB 050509B (redshift  $z \simeq 0.22$ ); we mark this constraint in Figure 13 with an arrow. For  $M_{\text{tot}} = 0.1M_{\odot}$  this constrains the ejected Ni mass to be  $M_{\text{Ni}} \lesssim 10^{-2}M_{\odot}$  (see also Kulkarni 2005). As Figure 12 illustrates, compact object mergers are very unlikely to produce this much Ni, so the absence of a detection thus far is unsurprising.

## 6 CONCLUSION AND DISCUSSION

We have calculated the time-dependent evolution of accretion disks formed from compact mergers, and the properties of their outflows. Since most of the disk mass resides at large radii, we approximate the disk as a ring at a given radius and calculate the dynamics and composition of the ring as a function of time. This ring model is calibrated to correctly reproduces the Green’s function solution for a viscously spreading ring with viscosity  $\nu \propto r^{1/2}$  (appropriate for a thick disk; see Appendix A). With this simplified model, we have studied the full parameter space of remnant accretion disks (different initial masses, compositions, etc.) and can follow the viscous evolution for arbitrarily long timescales.

The energetics of the ring at a given time can be described by one of three models: (1) optically thick to neutrinos and advective, (2) optically thin to neutrinos and geometrically thin, and (3) optically thin to neutrinos and advective. A massive, compact disk (with a short initial viscous time  $t_{\text{visc},0}$ ; eq. [5]) will exhibit all three of these accretion phases, evolving from (1) to (3) as a function of time (Figs. 1-4). Less massive disks, on the other hand, only pass through phases (2) and (3), or even just (3). Note that these phases refer to the energetics of the disk near the outer radius. At a given time, the disk may also undergo similar transitions as a function of radius; e.g., a disk that is advective at large

radii will be neutrino cooled and geometrically thin inside the ignition radius  $r_{\text{ign}}$  (eq. [19]).

Neutrino-driven winds during the early-time optically thick and neutrino-cooled (thin disk) phases unbind so much mass that field lines connected to the disk cannot produce sufficiently relativistic material to power short-duration GRBs (§5.1 and Fig. 10). An alternative source for the relativistic material needed to produce short GRBs are nearly baryon-free magnetic field lines that thread the BH's event horizon (e.g., McKinney 2005). In addition, when the inner disk becomes advective ( $\dot{M}_d \lesssim 0.07 \alpha_{0.1}^{5/3} M_\odot \text{s}^{-1}$  for  $\alpha = 0$ ), conditions appear particularly suitable for the formation of relativistic jets (by analogy to X-ray binaries, which produce jets when making a similar transition; e.g., Remillard & McClintock 2006; see Lazatti et al. 2008 for a similar argument in the context of long-duration GRBs).

Once the disk has transitioned to a late-time advective phase (phase 3 above), the properties of the disk become well-described by self-similar solutions. Ignoring for the moment outflows from the disk, these solutions are  $r_d \propto t^{2/3}$ ,  $M_d \propto t^{-1/3}$ , and  $\dot{M}_d \propto t^{-4/3}$ . Power-law variations in the disk properties are a generic feature of a viscously evolving disk that conserves total angular momentum. These scalings are not, however, likely to be applicable in practice because outflows during the advective phase unbind most of the remaining material (§4.1 & 5.2). Energy produced by fusion to He and heavier elements also contributes to driving an outflow (Figs. 3 & 4). Such outflows remove a significant fraction of the angular momentum of the disk. This leads to a much more rapid decrease in the disk mass and accretion rate at late times (Appendix B3 and Fig. 6). Significant accretion onto the central black hole will thus only last for a few viscous times after the onset of the advective phase.

At the outer edge of the disk, the transition from a neutrino-cooled thin disk to the late-time advective phase occurs at a time  $t_{\text{thick}} \sim 0.1 \alpha_{0.1}^{-23/17} (J_{49}/2)^{9/17} \text{ s}$  (eq. [20]). The rapid decrease in  $\dot{M}_d$  after the onset of the advective phase implies that the inner disk becomes advective at a similar time (§5.2 and Fig. 6). Quantitatively, we find that for powerful winds with  $p = 1$  (see eq. [B8]), the inner disk becomes advective at  $t \sim 0.2, 5,$  and  $100 \text{ sec}$ , for  $\alpha = 0.1, 0.01,$  and  $0.001$ , respectively (for our fiducial model with an initial mass of  $0.1 M_\odot$  and an initial radius of  $\simeq 3 \times 10^7 \text{ cm}$ ). Thus, for  $\alpha \sim 10^{-3}$ , the timescale for the inner disk to become advective is comparable to the onset of observed flaring at  $\sim 30 \text{ sec}$  in some short GRBs (e.g., Berger et al. 2005). Given the slow decline in disk mass with time before  $t_{\text{thick}}$ , there is ample accretion energy available in the disk at this point to power the observed flaring. However, there is observational evidence for  $\alpha \sim 0.1$  in a number of astrophysical disks (King et al. 2007); we thus doubt that  $t_{\text{thick}}$  is large enough to coincide with the onset of observed flaring. Instead  $t_{\text{thick}}$  is likely to be  $\sim 0.1 - 1 \text{ sec}$ , comparable to the duration of the short GRB itself. In this case, the rapid decrease in the disk mass and accretion rate in the advective phase imply that the remnant accretion disk alone does not contain sufficient mass at  $\sim 30 \text{ sec}$  to power the observed late-time activity from short GRBs, nor is there any physical reason to expect a sudden change in the disk or jet properties at this time.

A more likely source of late-time flaring in compact object merger models is a continued inflow of mass at late times, such as is produced by the infalling tidal tail found

in Lee & Ramirez-Ruiz's (2007) NS-NS merger simulations (see also Rosswog 2007). Similarly, the BH-NS merger simulations of Faber et al. (2006a,b) show that  $\sim 0.03 M_\odot$  of material is ejected into highly eccentric orbits during the merger, which returns to the BH on a timescale  $\gtrsim 1 \text{ s}$ . However, final conclusions regarding the quantity and ubiquity of late-time fall-back from NS-NS and BH-NS mergers must await full-GR simulations which include BH spin and realistic EOSs.

The second major focus of this paper has been on the composition of the accretion disk and its outflows as a function of time. For initial disk properties expected in compact object mergers (§2), the disk typically comes into  $\beta$ -equilibrium given the high temperatures and densities at small radii. As material spreads to larger radii, however, the composition of the disk freezes out before it becomes advective at late times; at freeze-out the disk is modestly neutron rich, with an electron fraction  $Y_e \approx 0.3$  (§4.2 and Fig. 9). This neutron rich material –  $\sim 10^{-2} M_\odot$  for typical initial disk parameters – is blown away once the disk enters the advective phase at  $\sim t_{\text{thick}}$ . These outflows are particularly interesting given the low solar system abundance of material produced in nuclear statistical equilibrium at  $Y_e \sim 0.3$  (Hartmann et al. 1985). In a separate paper, we will study this nucleosynthesis and its implications in more detail.

Although outflows from compact object merger accretion disks are neutron rich in most circumstances, neutrino-driven winds from radii  $\simeq 10^6 - 10^7 \text{ cm}$  at accretion rates  $\dot{M}_d \sim 0.03 - 1 M_\odot \text{s}^{-1}$  have electron fractions  $Y_e \simeq 0.5$ , precisely that required to synthesize significant amounts of  $^{56}\text{Ni}$  (Fig. 11). We have calculated the total Ni mass ejected by compact object merger disks as a function of their initial mass and radius (§5.4 and Fig. 12). Disks with initial masses  $\gtrsim 0.1 M_\odot$  can produce up to  $\sim 10^{-3} M_\odot$  of  $^{56}\text{Ni}$ . The radioactive decay of this Ni as the outflow expands to large radii will produce an optical and infrared transient peaking  $\sim 0.5 - 2 \text{ days}$  after the merger, with a peak flux of  $\nu L_\nu \simeq 10^{40} \text{ ergs s}^{-1}$  (Fig. 13). Because the Ni mass is likely to be a small fraction of the total mass of the ejecta (most of which is neutron rich), this transient is best detected at  $\sim 1 \mu\text{m}$ . As Figure 13 shows, current observational limits on SN-like transients coincident with short GRBs are about a factor of  $\sim 10$  above our predictions. However, somewhat deeper limits from a moderately closer burst could start to put interesting constraints on short GRB progenitors. It is also possible that the decay of some neutron-rich isotopes could heat the outflow and contribute to the late-time thermal emission (although most such isotopes have very short half-lives). This possibility should be investigated in future calculations using a nuclear reaction network.

Although we have focused on short GRBs throughout this paper, many of our results can be applied more broadly. For example, long duration GRBs show late-time activity and flaring similar to that seen in short GRBs (e.g., Falcone et al. 2007). For the reasons described above, this activity is probably produced by a continued inflow of mass at late times (fallback from the stellar progenitor's envelope) rather than solely by the viscous evolution of the small-scale disk. As a final application of our results, we note that the accretion-induced collapse of a white dwarf to a neutron star (AIC) is expected to produce a compact disk of  $\sim 0.1 - 0.5 M_\odot$  outside the newly formed neutron star's sur-

face (Dessart et al. 2006). The calculations presented here describe the evolution of this remnant disk, with the one caveat that the composition of the disk in the AIC context may be strongly affected by neutrino irradiation from the newly-formed neutron star.

## ACKNOWLEDGMENTS

We thank Josh Bloom, Davide Lazzati, and Daniel Perley for useful conversations. A. L. P. is supported by the Theoretical Astrophysics Center at UC Berkeley. B. D. M. and E. Q. are supported in part by the David and Lucile Packard Foundation, NASA Grant NNG06GI68G, and a NASA GSRP Fellowship to B.D.M.

## APPENDIX A: CALIBRATION OF THE RING MODEL

The surface density  $\Sigma$  of an axisymmetric disk in a Keplerian potential with constant total angular momentum evolves according to a diffusion equation (e.g., Frank et al. 2002):

$$\frac{\partial \Sigma}{\partial t} = \frac{3}{r} \frac{\partial}{\partial r} \left[ r^{1/2} \frac{\partial}{\partial r} (\nu \Sigma r^{1/2}) \right], \quad (\text{A1})$$

where  $\nu$  is the kinematic viscosity. Assuming that  $\nu$  depends only on radius as a power law, viz:  $\nu = \nu_0 (r/R_0)^n$ , equation (A1) is linear and, for an initial surface density distribution  $\Sigma(r, t=0) = (M_0/2\pi R_0) \delta(r-R_0)$  which is narrowly peaked about the radius  $R_0$ , the solution (for  $n < 2$ ) is given by

$$\Sigma(r, t) = \frac{M_0(1-n/2)}{\pi R_0^2 x^{(n+1/4)\tau}} \exp \left[ \frac{-(1+x^{2-n})}{\tau} \right] I_{1/|4-2n|} \left[ \frac{2x^{1-n/2}}{\tau} \right], \quad (\text{A2})$$

where  $M_0$  is the initial disk mass,  $x \equiv r/R_0$ ,  $\tau \equiv t[12\nu_0(1-n/2)^2/R_0^2]$ , and  $I_m$  is a modified Bessel function of order  $m$ . For small argument  $y \ll 1$ ,  $I_m(y)$  takes the asymptotic form  $I_m \simeq (y/2)^m/\Gamma(m+1)$ , where  $\Gamma$  is the Gamma function; thus, for late times or small radii such that  $\tau \gg 2x^{1-n/2}$ , equation (A2) reduces to

$$\Sigma(r, t) \Big|_{\tau \gg 2x^{1-n/2}} = \frac{M_0}{\pi R_0^2} \frac{(1-n/2)}{\Gamma[\frac{5-2n}{4-2n}]} \frac{1}{\tau^{(\frac{5-2n}{4-2n})x^n}} \exp \left[ \frac{-(1+x^{2-n})}{\tau} \right] \quad (\text{A3})$$

Most of the mass in the disk is located near the radius where the local mass  $M_d \propto \Sigma r^2$  peaks; using equation (A3), at late times this radius is found to be  $r_{\text{peak}} = R_0 \tau^{1/(2-n)}$ . Hence, equation (A3) becomes valid near  $r_{\text{peak}}$  for  $\tau \gg 1$ .

The constant  $A$ , which relates the total disk mass at late times from the exact solution of equation (A1) to the mass defined by  $\pi \Sigma(r_{\text{peak}}) r_{\text{peak}}^2$ , can be calculated from equation (A3) to be

$$A(\tau \gg 1) \equiv \frac{\int_0^\infty 2\pi \Sigma r dr}{\pi \Sigma(r_{\text{peak}}) r_{\text{peak}}^2} \Big|_{\tau \gg 1} = \frac{2e}{2-n} \quad (\text{A4})$$

Similarly, the constant  $B$ , which relates the total disk angular momentum at late times from the exact solution to that estimated by  $\pi \Sigma r_{\text{peak}}^2 (GM r_{\text{peak}})^{1/2}$ , is given by

$$B(\tau \gg 1) \equiv \frac{\int_0^\infty 2\pi \Sigma r^{3/2} dr}{\pi \Sigma(r_{\text{peak}}) r_{\text{peak}}^{5/2}} \Big|_{\tau \gg 1} = \frac{2e}{2-n} \Gamma \left[ \frac{5-2n}{4-2n} \right] \quad (\text{A5})$$

From mass continuity, the radial velocity is given by

$$v_r = \frac{-3}{\Sigma r^{1/2}} \frac{\partial}{\partial r} [\nu \Sigma r^{1/2}] = \frac{-3\nu_0}{R_0} \frac{1}{\Sigma x^{1/2}} \frac{\partial}{\partial x} [\Sigma x^{n+1/2}], \quad (\text{A6})$$

which, using equation (A3), gives the accretion rate at small radii

$$\begin{aligned} \dot{M}_{\text{in}} &= -2\pi \Sigma r v_r \Big|_{\tau \gg 2x^{1-n/2}} \\ &= \frac{M_0}{R_0^2/\nu_0} \frac{3(1-n/2)}{\Gamma[(5-2n)/(4-2n)]} \exp[-1/\tau] \tau^{-\frac{(5-2n)}{(4-2n)}} \end{aligned} \quad (\text{A7})$$

Equation (A7) is easily checked by noting that  $\int_0^\infty \dot{M}_{\text{in}} dt = M_0$ , which shows that the entire initial disk eventually accretes onto the central object. In §3.1 we introduced the following prescription for evolving the disk mass:

$$\dot{M}_d = \frac{f M_d}{t_{\text{visc}}}, \quad (\text{A8})$$

where, in terms of the viscosity prescription adopted above,  $t_{\text{visc}} = r_d^2/\nu = t_{\text{visc},0} (r_d/R_0)^{2-n}$  and  $t_{\text{visc},0} \equiv R_0^2/\nu_0$  is the initial viscous time. Assuming that the total disk angular momentum remains constant,  $J \propto M_d r_d^{1/2} = M_0 R_0^{1/2}$ , the solution to equation (A8) is given by

$$M_d(t) = M_0 [1 + (4-2n)f(t/t_{\text{visc},0})]^{-1/(4-2n)} \quad (\text{A9})$$

In our evolutionary calculations we set  $f$  so that the accretion rate from the exact solution to equation (A1) ( $\dot{M}_{\text{in}}$ ; eq. [A7]) matches the solution to equation (A8) at late times (i.e., in the self-similar limit). This requires

$$f = 3(1-n/2)\Gamma[(5-2n)/(4-2n)]^{4-2n} \quad (\text{A10})$$

For an advection-dominated disk,  $\nu = \alpha c_s H \propto \Omega R^2 \propto r^{1/2}$ ; thus,  $n = 1/2$ ,  $f \simeq 1.602$ ,  $A \simeq 3.62$ , and  $B \simeq 3.23$ . For a neutrino-cooled, optically-thin disk which is dominated by gas pressure,  $T \propto r^{-3/10}$  and  $\nu \propto r^{6/5}$ ; thus,  $n = 6/5$ ,  $f \simeq 1.01$ ,  $A \simeq 6.80$ , and  $B \simeq 6.09$ .

In Figure A1 we show  $\dot{M}_{\text{in}}/\dot{M}_d$  as a function of  $t/t_{\text{visc},0}$  for  $n = 1/2$  in order to compare the disk evolution derived from the exact solution of equation (A1) to that calculated from our simplified model. Figure A1 also shows the ratio of the total disk mass  $M_{\text{tot}} \equiv \int_0^\infty 2\pi \Sigma r dr$  calculated from equation (A2) to the disk mass  $M_d$  (eq. [A9]) of the simplified model, as well as the ratio of  $r_{\text{peak}}$  (the radius where  $\Sigma r^2$  peaks, using eq. [A2] for  $\Sigma$ ) to the radius determined by angular momentum conservation:  $r_d = R_0 (M_d/M_0)^2$ . Figure A1 shows that, although the accretion rate in the two models differ at very early times (the initially narrowly-concentrated ring takes a short period of time to spread to small radii), they approach one another to  $\lesssim 20\%$  by  $t \gtrsim 0.1 t_{\text{visc},0}$ . Likewise, the disk mass and radii from the exact solution and simplified model are quite similar at all times.

The numerical values for  $A$  and  $B$  given in equations (A4) and (A5) and employed in our calculations apply only to the mass and angular momentum distribution in the disk at late times ( $\tau \gg 1$ ). Initially, the disk is entirely concentrated at a single radius and  $A(t=0) = B(t=0) = 1$ ; thus,  $A(t)$  and  $B(t)$  evolve significantly from early times until the disk enters the self-similar limit and so one might worry that the early-time description of the disk's evolution depends

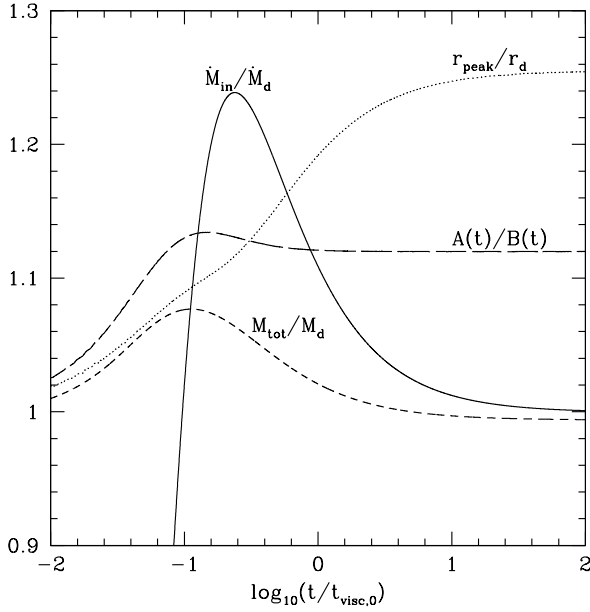


**Figure A1.** Comparison of the accretion rate (*solid*), disk mass (*short dashed*), and disk radius (where the local disk mass peaks; *dotted*) as calculated from our simplified ring model to that derived from the exact solution of the diffusion equation for a  $\delta$ -function initial mass distribution (eq. [A2]); we assume  $\nu \propto r^{1/2}$ , as applies for a thick disk. The parameter  $f \simeq 1.6$  (eq. [A10]) adopted in our model is chosen to ensure that the accretion rates match at late times (i.e.,  $\dot{M}_{\text{in}}/\dot{M}_d \rightarrow 1$ ). Also shown is the ratio  $A(t)/B(t)$  (eqs. [A4] and [A5]), a measure of the relative distribution of mass and angular momentum, which asymptotes to  $\Gamma[(5-2n)/(4-2n)] \simeq 1.12$  at late times.

sensitively on the initial mass distribution. Our model only assumes, however, that the *ratio*  $A(t)/B(t)$  remains constant, which is a good approximation. To illustrate this, Figure A1 shows  $A(t)/B(t)$  calculated from the exact solution (eq. [A2]) for  $n = 1/2$ . Note that  $A(t)/B(t)$  increases from unity to its asymptotic value  $A/B = \Gamma[(5-2n)/(4-2n)]$ , which is  $\simeq 1.12$  for  $n = 1/2$ .

## APPENDIX B: ANALYTIC SELF-SIMILAR SOLUTIONS

The late-time evolution of our disk calculations asymptote to power laws that are well approximated by analytic self-similar solutions. We derive these here to aid in interpreting our numerical results. Presentation is divided between neutrino-cooled, thin-disk solutions and late-time advective solutions. One could just as well derive analogous results for disks that are optically thick to neutrinos. We forgo this here since the initial viscous time is always sufficiently long that these solutions are never applicable to our numerical results. We conclude by presenting self-similar solutions for advective disks with substantial mass loss, since these differ significantly from the solutions without mass loss.

### B1 Neutrino-cooled, Thin-disk Solutions

In the neutrino-cooled, thin-disk limit, the cooling is dominated by Urca, and the pressure is given by ideal gas. Combining local energy balance and continuity,  $\dot{M}_d = fA\pi\nu\Sigma$ , allows us to solve for the temperature and column density as functions of radius. We substitute these into the angular momentum equation,  $B(GMr_d)^{1/2}\pi r_d^2\Sigma = J_d$ , to solve for  $M_d$  as a function of  $\dot{M}_d$  and  $J_d$ . We then assume the solutions have a self-similar form of  $M_d \propto t^{-\beta}$ , so that  $\dot{M}_d = -dM_d/dt = \beta M_d/t$ . In this way we solve for  $\beta = 5/8$ ,  $\dot{M}_d(t)$ , and subsequently any other variable of interest. The results are

$$M_d =$$

$$1.3 \times 10^{-2} f_{1.6}^{-5/8} \left( \frac{A_{3.6}}{B_{3.2}} \right) \alpha_{0.1}^{-3/4} M_3^{-1/4} \left( \frac{J_{49}}{2} \right) t^{-5/8} M_\odot, \quad (\text{B1})$$

$$\dot{M}_d =$$

$$2.7 \times 10^{-2} f_{1.6}^{-5/8} \left( \frac{A_{3.6}}{B_{3.2}} \right) \alpha_{0.1}^{-3/4} M_3^{-1/4} \left( \frac{J_{49}}{2} \right) t^{-13/8} M_\odot \text{s}^{-1} \quad (\text{B2})$$

and

$$r_d = 4.1 \times 10^8 f_{1.6}^{5/4} \alpha_{0.1}^{3/2} M_3^{-1/2} t^{5/4} \text{cm}. \quad (\text{B3})$$

where  $f_{1.6} = f/1.6$ ,  $A_{3.6} = A/3.6$ ,  $B_{3.2} = B/3.2$ , and  $t$  is measured in seconds, and the prefactors have been scaled to match our numerical results. The first thing to notice is that both  $M_d$  and  $\dot{M}_d$  are rather insensitive to the choice of  $f$  as long as it is near unity, and  $A$  and  $B$  only appear as a ratio, which is also nearly unity. This provides confidence in using this parameterization, and these specific values for the corresponding parameters, when the disk is not well-described by  $n = 1/2$ . This analysis also demonstrates the relative dependence on  $\alpha$ . In Figure B1 we compare these scaling (*dotted lines*) with the numerical calculations. This shows that these solutions are only applicable for a short time. At times when  $t < t_{\text{visc}}$  the evolution is much flatter and is dominated by initial conditions. At later times the disk becomes advective and the solutions of the next section apply.

### B2 Late-time Advective Solutions

In this limit, self-similar solutions can be found in an analogous way. The viscous energy release is carried by advection with the internal energy dominated by relativistic particles, so that

$$\frac{9}{8fA\pi} \Omega^2 \dot{M} = V_r \frac{H}{r} \frac{11}{6} aT^4. \quad (\text{B4})$$

Combining this with mass continuity, gives the column depth as a function of radius,  $\Sigma(r) = (16/9A\pi\alpha)(\dot{M}/r^2\Omega)$ . We then use this relation with  $B(GMr_d)^{1/2}M_d = J_d$  and  $\dot{M}_d = \beta M_d/t$ , to find  $\beta = 1/3$  and the self-similar solutions

$$M_d = 3.7 \times 10^{-2} \left( \frac{A_{3.6}}{B_{3.2}} \right) \alpha_{0.1}^{-1/3} M_3^{-2/3} \left( \frac{J_{49}}{2} \right) t^{-1/3} M_\odot, \quad (\text{B5})$$

$$\dot{M}_d = 1.2 \times 10^{-2} \left( \frac{A_{3.6}}{B_{3.2}} \right) \alpha_{0.1}^{-1/3} M_3^{-2/3} \left( \frac{J_{49}}{2} \right) t^{-4/3} M_\odot \text{s}^{-1}, \quad (\text{B6})$$

and



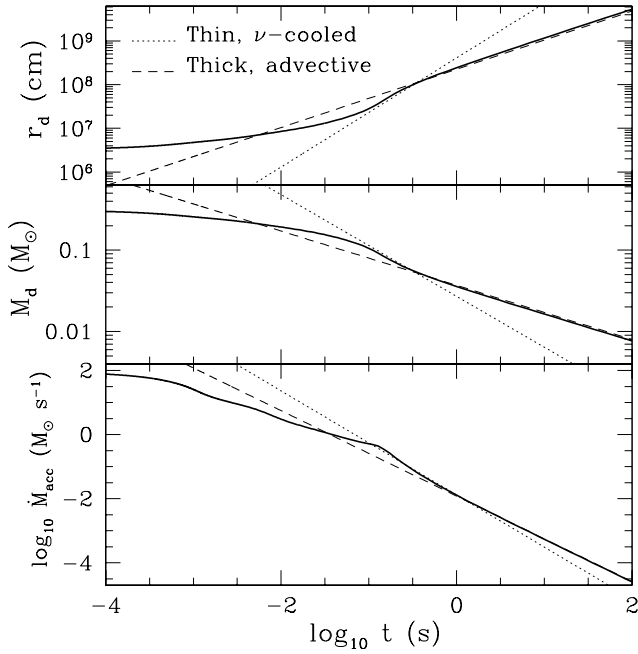


**Figure B1.** Comparison of the numerical disk solutions (*solid lines*) with the analytic solutions for the thin, neutrino-cooled (*dotted lines*) and thick, advective limits (*dashed lines*). The numerical solution is the  $0.3M_{\odot}$  disk from Fig. 1.

$$r_d = 2.3 \times 10^8 \alpha_{0.1}^{2/3} M_3^{1/3} t^{2/3} \text{ cm.} \quad (\text{B7})$$

These advective results are even more insensitive to  $A$ ,  $B$ , and  $f$  than the thin-disk results. Equation (B5)-(B7) are plotted in Figure B1 as dashed lines. The numerical calculations follow these solutions very closely for times later than  $t_{\text{thick}}$  (given by eq. [20]).

Equations (B5)-(B7) can also be derived ignoring equation (B4), but assuming that the scaleheight is fixed at  $H/r \simeq 0.6$ . This introduces the additional dependencies  $M_d \propto (H/r)^{-2/3}$ ,  $\dot{M}_{\text{acc}} \propto (H/r)^{-2/3}$ , and  $r_d \propto (H/r)^{4/3}$ , but gives nearly identical prefactors.

### B3 Advective Solutions with Mass Loss

In §5.2 we described how advective disks are likely to lose a substantial fraction of their mass to viscously driven outflows. Because the outflow removes angular momentum as well – at least the specific angular momentum of the mass that is lost – the disk need not expand as rapidly to large radii. In addition, the disk mass and accretion rate decrease much more rapidly at late times than in the self-similar solutions described in the previous subsection. To quantify this effect, we follow Blandford & Begelman (1999) and assume that only a fraction  $\sim (r_*/r_d)^p$  of the available material is accreted onto the central BH. The remainder is lost to an outflow. Thus the outflow rate at any time is given by

$$\dot{M}_{\text{out}} = \left(1 - \left[\frac{r_*}{r_d}\right]^p\right) \frac{f M_d}{t_{\text{visc}}} \quad (\text{B8})$$

We further assume that the angular momentum loss rate from the disk is given by

$$\dot{J} = -C \dot{M}_{\text{out}} (GM r_d)^{1/2}. \quad (\text{B9})$$

where  $C$  is a constant that depends on the torque exerted by the outflowing mass on the remaining disk. If the outflow produces no net torque, an assumption that appears at least qualitatively consistent with the relatively small-scale magnetic fields seen in global MHD disk simulations (e.g., Stone & Pringle 2001), then the angular momentum loss is only that due to the specific angular momentum of the outflow, and (Kumar, Narayan, & Johnson 2008)

$$C = \frac{2p}{2p+1}. \quad (\text{B10})$$

We solve equations (6), (7), (B8), and (B9), assuming  $A/B = 1$  and  $\nu \propto r^{1/2}$  (as appropriate for a thick disk). The solution depends on the relative magnitude of  $1 - C$  and  $C(r_*/r_d)^p$ . For  $C(r_*/r_d)^p \ll 1 - C$ , which is true at nearly all times if equation (B10) is applicable, then

$$r_d \simeq r_{d,0} \left[1 + 3f(1 - C) \left(\frac{t}{t_{\text{visc},0}}\right)\right]^{2/3}, \quad (\text{B11})$$

$$M_d \simeq M_{d,0} \left[1 + 3f(1 - C) \left(\frac{t}{t_{\text{visc},0}}\right)\right]^{-1/[3(1-C)]}, \quad (\text{B12})$$

and

$$\dot{M}_{\text{in}} \simeq f \frac{M_{d,0}}{t_{\text{visc},0}} \left(\frac{r_*}{r_{d,0}}\right)^p \times \left[1 + 3f(1 - C) \left(\frac{t}{t_{\text{visc},0}}\right)\right]^{-[1+3(1+2p/3)(1-C)]/[3(1-C)]} \quad (\text{B13})$$

Note that if  $p = C = 0$  (i.e., no mass or angular momentum loss), then these self-similar solutions reduce to those of the previous subsection. However, for the case  $p = 1$  consistent with a number of global advective disk simulations (e.g., Hawley & Balbus 2002), and in the absence of a net torque on the disk,  $C = 2/3$  and these solutions correspond to  $r_d \propto t^{2/3}$ ,  $M_d \propto t^{-1}$ , and  $\dot{M}_{\text{in}} \propto t^{-8/3}$  (see also Fig. 6). This shows that the disk mass and accretion rate decrease substantially more rapidly in time than in the absence of an outflow, while the disk expands outward at roughly the same rate. If there is a net torque on the disk such that  $C \simeq 1$ , then equations (B11)-(B13) are not applicable. Instead, for  $C(r_*/r_d)^p \gg 1 - C$ , the solution is given by (for  $p \neq 0$  and  $t \gg t_{\text{visc},0}$ )

$$r_d(t) \simeq [(3 + 2p) f r_*^p r_{d,0}^{1.5}]^{1/(1.5+p)} \left(\frac{t}{t_{\text{visc},0}}\right)^{1/(1.5+p)} \quad (\text{B14})$$

and

$$M_d(t) \simeq M_{d,0} \exp[-D(t/t_{\text{visc},0})^{p/(1.5+p)}] \quad (\text{B15})$$

where

$$D = \left(\frac{1.5 + p}{p(3 + 2p)^{1.5/(1.5+p)}}\right) \left(\frac{f r_{d,0}^{1.5}}{[f r_*^p r_{d,0}^{1.5}]^{1.5/(1.5+p)}}\right). \quad (\text{B16})$$

For  $p = 1$  and for  $r_{d,0} \sim r_*$ , these solutions become  $r_d(t) \sim r_{d,0}(t/t_{\text{visc},0})^{2/5}$  and  $M_d(t) \sim M_{d,0} \exp[-1.15(t/t_{\text{visc},0})^{2/5}]$ . The radius of the disk thus increases significantly more slowly, and the mass of the disk decreases much more rapidly, than in the self-similar solutions without mass-loss.

The numerical solutions including mass-loss during the advective phase shown in §4.1 (Fig. 6) assume that equation (B10) is applicable and are indeed well-described by

the self-similar solutions given in equations (B11)-(B13) at late times.

## REFERENCES

- Barthelmy, S. D., et al. 2005, *Nature*, 438, 994
- Barzilai, Y., & Levinson, A. 2008, *New Astronomy*, 13, 386
- Baumgarte, T. W., Shapiro, S. L., & Shibata, M. 2000, *ApJL*, 528, L29
- Beloborodov, A. M. 2003, *ApJ*, 588, 931
- Beloborodov, A. M. 2003b, *ApJL*, 585, L19
- Berger, E., et al. 2005, *Nature* 438, 988
- Bildsten, L. & Cutler, C. 1992, *ApJ*, 400, 175
- Blandford, R. D., & Begelman, M. C. 1999, *MNRAS*, 303, L1
- Bloom, J. S., et al. 2006, *ApJ*, 638, 354
- Campana, S., et al. 2006, *A&A*, 454, 113
- Chen, W. X. & Beloborodov, A. M. 2007, *ApJ*, 657, 383 (*CB07*)
- Colgate, S. A., Petschek, A. G., & Kriese, J. T. 1980, *ApJL*, 237, L81
- Dai, Z. G., et al. 2006, *Science*, 311, 1127
- Daigne, F., & Mochkovitch, R. 2002, *A&A*, 388, 189
- Derishev, E. V., Kocharovsky, V. V., & Kocharovsky, V. V. 1999, *ApJ*, 521, 640
- Dessart, L., Burrows, A., Ott, C. D., Livne, E., Yoon, S.-C., & Langer, N. 2006, *ApJ*, 644, 1063
- Dessart, L., Burrows, A., Livne, E., & Ott, C. D. 2008a, *ApJL*, 673, L43
- Dessart, L., Ott, C., Burrows, A., Rosswog, S., & Livne, E. 2008b, *ArXiv e-prints*, 806, arXiv:0806.4380
- DiMatteo, T., Perna, R., & Narayan, R. 2002, *ApJ*, 579, 706
- Duez, M. D., Liu, Y. T., Shapiro, S. L., Shibata, M., & Stephens, B. C. 2006, *Phys. Rev. D*, 73, 104015
- Duez, M. D., Liu, Y. T., Shapiro, S. L., & Stephens, B. C. 2004, *Phys. Rev. D*, 69, 104030
- Eichler, D., Livio, M., Piran, T., & Schramm, D. N. 1989, *Nature*, 340, 126
- Faber, J. A., et al. 2006a, *Phys. Rev. D*, 73, 4012
- Faber, J. A., et al. 2006b, *ApJ*, 641, L93
- Falcone, A. D., et al. 2007, *ApJ*, 671, 1921
- Ferrero, P., et al. 2007, *AJ*, 134, 2118
- Fishbone, L. G. 1973, *ApJ*, 185, 43
- Fox, D. B., et al. 2005, *Nature*, 437, 845
- Frank, J., King, A. R., & Raine, D. J. 2002, *Accretion Power in Astrophysics* (3d ed.; Cambridge: Cambridge Univ. Press)
- Freiburghaus, C., Rosswog, S., & Thielemann, F.-K. 1999, *ApJL*, 525, L121
- Galama, T. J., et al. 1998, *Nature*, 385, 670
- Gehrels, N. et al. 2005, *Nature*, 437, 851
- Haensel, P., & Zdenek, J. L. 1990a, *A&A*, 227, 431
- Haensel, P., & Zdenek, J. L. 1990b, *A&A*, 229, 117
- Hartmann, D., Woosley, S. E., & El Eid, M. F. 1985, *ApJ*, 297, 837
- Hawley, J. F., & Balbus, S. A. 2002, *ApJ*, 573, 738
- Hjorth, J., et al. 2003, *Nature*, 423, 847
- Hjorth, J., et al. 2005, *ApJL*, 630, L117
- Janiuk, A., Perna, R., DiMatteo, T., & Czerny, B. 2004, *MNRAS*, 355, 950
- Janka, H.-Th., Eberl, T., Ruffert, M., & Fryer, C. L. 1999, *ApJ*, 527, L39
- King, A. R., et al. 2005, *ApJ*, 630, L113
- King, A. R., Pringle, J. E., & Livio, M. 2007, *MNRAS*, 376, 1740
- Kluźniak, W. & Lee, W. H. 1998, *ApJ*, 494, L53
- Kohri, K. & Mineshige, S. 2002, *ApJ*, 577, 311
- Kopal, Z. 1959, *Close Binary Systems* (London: Chapman & Hall)
- Krolik, J. H., Hirose, S., & Blaes, O. 2007, *ApJ*, 664, 1045
- Kulkarni, S. R. 2005, *ArXiv Astrophysics e-prints*, arXiv:astro-ph/0510256
- Kumar, P., Narayan, R., & Johnson, J. L. 2008, *ArXiv e-prints*, 807, arXiv:0807.0441
- Lai, D., Rasio, F. A., & Shapiro, S. L. 1994, *ApJ*, 423, 344
- La Parola, V., et al. 2006, *A&A*, 454, 753
- Lattimer, J. M., & Schramm, D. N. 1974, *ApJL*, 192, L145
- Lazzati, D., Ramirez-Ruiz, E., & Ghisellini, G. 2001, *A&A*, 379, L39
- Lazzati, D., Perna, R., & Begelman, M. C. 2008, *ArXiv e-prints*, 805, arXiv:0805.0138
- Lee, W. H. & Kluźniak, W. 1995, *Acta Astron.*, 45, 705
- Lee, W. H. & Kluźniak, W. 1998, *ApJ*, 526, 178
- Lee, W. H. & Kluźniak, W. 1999, *MNRAS*, 308, 780
- Lee, W. H., Ramirez-Ruiz, E., & Page, D. 2004, *ApJL*, 608, L5
- Lee, W. & Ramirez-Ruiz, E. 2007, *New J. Phys.*, 9, 17
- Lee, W. H., Ramirez-Ruiz, E., & Page, D. 2004, *ApJ*, 608, L5
- Lee, W. H., Ramirez-Ruiz, E., & Page, D. 2005b, *ApJ*, 632, 421
- Lemoine, M. 2002, *A&A*, 390, L31
- Levinson, A. 2006, *ApJ*, 648, 510
- Li, L.-X., & Paczyński, B. 1998, *ApJL*, 507, L59
- McKinney, J. C. 2005, *ArXiv Astrophysics e-prints*, arXiv:astro-ph/0506368
- Metzger, B. D., Thompson, T. A., & Quataert, E. 2008b, *ApJ*, 676, 1130 (*M08B*)
- Montanari, E., et al. 2005, *ApJ*, 625, L17
- Morrison, I. A., Baumgarte, T. W., & Shapiro, S. L. 2004, *ApJ*, 610, 941
- Nakar, E. 2007, *Phys. Rep.*, 442, 166
- Narayan, R., Piran, T., & Kumar, P. 2001, *ApJ*, 557, 949
- Narayan, R., Piran, T., & Shemi, A. 1991, *ApJ*, 379, L17
- Oechslin, R., & Janka, H.-Th. 2006, *MNRAS*, 368, 1489
- Paczyński, B. 1986, *ApJ*, 308, L43
- Paczyński, B. 1991, *Acta Astron.*, 41, 257
- Perna, R., Armitage, P. J., & Zhang, B. 2005, *ApJ*, 636, L29
- Pethick, C. J., & Ravenhall, D. G. 1995, *Annu. Rev. Nucl. Part. Sci.*, 45, 429
- Piro, A. L. & Pfahl, E. 2007, *ApJ*, 658, 1173
- Popham, R., Woosley, S. E., & Fryer, C. L. 1999, *ApJ*, 518, 356
- Price, D. J., & Rosswog, S. 2006, *Science*, 312, 719
- Proga, D., & Begelman, M. C. 2003, *ApJ*, 592, 767
- Proga, D. & Zhang, B. 2006, *MNRAS*, 370, L61
- Pruet, J., Thompson, T. A., & Hoffman, R. D. 2004, *ApJ*, 606, 1006
- Qian, Y.-Z. 2000, *ApJL*, 534, L67
- Qian, Y.-Z., Fuller, G. M., Mathews, G. J., Mayle, R. W.,

- Wilson, J. R., & Woosley, S. E. 1993, *Physical Review Letters*, 71, 1965
- Qian, Y.-Z., & Woosley, S. E. 1996, *ApJ*, 471, 331 (*QW96*)
- Rasio, F. A., et al. 2005, *Proc. JGRG14 Yukawa Institute for Theoretical Physics* (preprint astro-ph/0503007)
- Rasio, F. A., & Shapiro, S. L. 1994, *ApJ*, 432, 242
- Remillard, R. A., & McClintock, J. E. 2006, *ARA&A*, 44, 49
- Rossi, E. M., Beloborodov, A. M., & Rees, M. J. 2006, *MNRAS*, 369, 1797
- Rosswog, S. 2007, *MNRAS*, 376, L48
- Rosswog, S., & Liebendörfer, M. 2003, *MNRAS*, 342, 673
- Rosswog, S., Speith, R., & Wynn, G. A., 2004, *MNRAS*, 351, 1121
- Ruffert, M., & Janka, H.-Th. 1999, *A&A*, 344, 573
- Ruffert, M., & Janka, H.-Th. 2001, *A&A*, 380, 544
- Ruffert, M., Janka, H.-Th., & Schäfer, G. 1996, *A&A*, 311, 532
- Ruffert, M., Janka, H.-Th., Takahashi, K., & Schäfer, G. 1997, *A&A*, 319, 122
- Setiawan, S., Ruffert, M., & Janka, H.-Th. 2004, *MNRAS*, 352, 753
- Setiawan, S., Ruffert, M., & Janka, H.-Th. 2006, *A&A*, 458, 553
- Shakura, N. I., & Sunyaev, R. A. 1973, *A&A*, 24, 337
- Shapiro, S. L., & Teukolsky, S. A. 1983, *Black Holes, White Dwarfs, and Neutron Stars: The Physics of Compact Objects* (New York: Wiley)
- Shibata, M., Taniguchi, K., & Uryū, K. 2005, *Phys. Rev. D*, 71, 084021
- Shibata, M. & Taniguchi, K. 2006, *Phys. Rev. D*, 73, 064027
- Soderberg, A. M., et al. 2006, *ApJ*, 650, 261
- Stanek, K. Z., et al. 2003, *ApJ*, 591, L17
- Stone, J. M., & Pringle, J. E. 2001, *MNRAS*, 322, 461
- Surman, R., McLaughlin, G. C., & Hix, W. R. 2006, *ApJ*, 643, 1057
- Surman, R., McLaughlin, G. C., Ruffert, M., Janka, H. -, & Hix, W. R. 2008, *ArXiv e-prints*, 803, arXiv:0803.1785
- Thompson, T. A., Burrows, A., & Meyer, B. S. 2001, *ApJ*, 562, 887
- Thompson, T. A., Chang, P., & Quataert, E. 2004, *ApJ*, 611, 380
- Uryū, K., & Eriguchi, Y. 1999, *MNRAS*, 303, 329
- Villasenor, J. S., et al. 2005, *Nature*, 437, 855
- Woosley, S. E. & Baron, E. 1992, *ApJ*, 391, 228
- Xie, Y., Huang, C.-Y., & Lei, W.-H. 2007, *Chinese Journal of Astronomy and Astrophysics*, 7, 685

